THE JOURNAL OF PHYSICAL CHEMISTRY A

ARTICLE

pubs.acs.org/JPCA

Influence of Water on Anharmonicity, Stability, and Vibrational Energy Distribution of Hydrogen-Bonded Adducts in Atmospheric Reactions: Case Study of the OH + Isoprene Reaction Intermediate Using Ab Initio Molecular Dynamics

Scott M. Dietrick, Alexander B. Pacheco, and Prasad Phatak

Department of Chemistry, Indiana University, Bloomington, Indiana 47405, United States

Philip S. Stevens

Department of Chemistry and Center for Research in Environmental Science, School of Public and Environmental Affairs, Indiana University, Bloomington, Indiana 47405, United States

Srinivasan S. Iyengar*

Departments of Chemistry and Physics, Indiana University, Bloomington, Indiana 47405, United States

ABSTRACT: The effect of water on the stability and vibrational states of a hydroxy-isoprene adduct is probed through the introduction of 1−15 water molecules. It is found that when a static nuclear harmonic approximation is invoked there is a substantial red-shift of the alcohol O−H stretch (of the order of 800 cm^{-1}) as a result of introduction of water. When potential energy surface sampling and associated anharmonicities are introduced through finite temperature ab initio dynamics, this hydroxy-isoprene OH stretch strongly couples with all the water vibrational modes as well as the hydroxy-isoprene OH bend modes. A new computational technique is introduced to probe the coupling between these modes. The method involves a two-dimensional, time-frequency analysis of the finite temperature vibrational properties. Such an analysis not only provides information about the modes that are coupled as a result of finite-temperature analysis, but also the temporal evolution of such coupling.

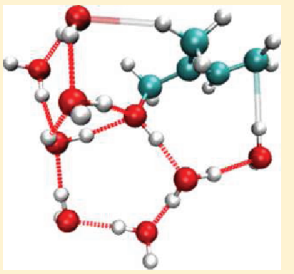

1. INTRODUCTION

The hydroxyl (OH) and peroxy radicals (HO_2 and RO_2) play a central role in the chemistry of the atmosphere. Through the oxidation of volatile organic compounds (VOCs), the OH radical initiates reactions that lead to the production of ozone and secondary aerosols in the atmosphere. Most of these reactions convert OH to both HO_2 and organic peroxy radicals (RO_2), which in the presence of nitrogen oxides (NO_x) typically found in urban areas are converted back to OH, resulting in a fast cycling of radicals that leads to the formation of ozone, the primary component of photochemical smog:

$$OH + VOC \rightarrow R + H_2O \quad (1a)$$

$$R + O_2 \rightarrow RO_2 \quad (1b)$$

$$RO_2 + NO \rightarrow RO + NO_2 \quad (1c)$$

$$RO_2 + NO \rightarrow RONO_2 \quad (1d)$$

$$HO_2 + NO \rightarrow OH + NO_2 \quad (1e)$$

$$NO_2 + h\nu \xrightarrow{O_2} NO + O_3 \quad (1f)$$

The situation is different on the regional scale, where ozone production tends to be limited by the lower concentration of NO_x,[1] resulting in self and cross reactions of peroxy radicals competing with reaction with NO, thus, terminating the radical chain according to

$$RO_2 + RO_2 \rightarrow 2RO + O_2 \quad (2a)$$

$$\rightarrow ROH + R'(O) + O_2 \quad (2b)$$

$$HO_2 + RO_2 \rightarrow ROOH + O_2 \quad (2c)$$

Measurements of OH and HO_2 can provide a critical test of our understanding of the fast photochemistry of these regions of the atmosphere.[2] However, many of these measurements show serious discrepancies with modeled concentrations of OH and HO_2, especially in forest environments dominated by isoprene emissions, bringing into question our understanding of the fast photochemistry of the troposphere and, specifically, the atmospheric chemistry of isoprene.[2−5] Unlike the OH-initiated oxidation of alkanes (reaction 1a), the OH-initiated reactions of unsaturated VOCs such as isoprene

Received: May 14, 2011
Revised: December 3, 2011
Published: December 05, 2011

involve OH addition to one of the carbon−carbon double bonds, resulting in the formation of hydroxy peroxy radicals:

$$OH + VOC \rightarrow R'OH(adduct) \quad (3a)$$

$$R'OH + O_2 \rightarrow HOR'O_2 \quad (3b)$$

$$HOR'O_2 + NO \rightarrow HOR'O + NO_2 \quad (3c)$$

To improve our understanding of the chemical mechanism of the OH-initiated oxidation of isoprene and other unsaturated VOCs, there have been several experimental measurements on the kinetics and mechanism of the OH-initiated oxidation of unsaturated VOCs such as isoprene and butadiene.[6] For such cases, it has recently been proposed[7] that several hydrogen-bonded peroxyl radicals could be formed as intermediates in the OH-initiated oxidation of isoprene. Furthermore, rearrangements of these peroxy radicals, through hydride, proton, or hydrogen atom shifts, followed by unimolecular decomposition or reaction with HO_2 can give rise to additional products, including HO_x radicals, aldehydes, and peroxols. Factors that govern the stability of such hydrogen-bonded systems may include enthalpic as well as entropic contributions, because some of these involve the formation of six- and eight-membered hydrogen-bonded rings.

The importance of these proposed peroxy radical reactions in the atmosphere depends on the rate of these peroxy radical isomerization reactions relative to the self- and cross-reactions of these peroxy radicals. Facilitating rate constants calculation studies for such complex systems are generally performed using the Rice−Ramsperger−Kassel−Marcus (RRKM) theory to compute unimolecular reaction rates. Computations on the vibrational partition function that appear in these rate equations are generally performed within the Harmonic approximation, where harmonic frequencies at optimized nuclear configurations or transition states lead to the appropriate density of states. This approach is, however, not adequate for systems that demonstrate soft modes, such as hydrogen bonds.[6,8−16] When hydrogen bonds facilitate reactions, shifts in transition states have been noted,[17] and these shifts are absent when the energies are computed within the harmonic approximation. These contributions are in addition to any anharmonicity contributions that may arise as a result of the floppy hydrogen-bond modes. For the atmospheric systems treated here, these effects will be explored in future publications. Through recent studies[8−14,18] the use of ab initio molecular dynamics (AIMD) to accurately represent vibrational properties of similar, soft-mode, hydrogen-bonded systems, in agreement with experiment, has been demonstrated (see, also, Appendix A). Some of these studies have included a detailed examination of H/D isotope effects, including their dependence on temperature.[6,12,13] In ref 19, the role of anharmonicity and energy redistribution on the vibrational states has been examined using similar approaches as those described in refs 6 and 9−13.

Furthermore, the influence of water on the stability and vibrational energy distribution in hydrogen-bonded reaction intermediates and transition states may be critical.[11,20−24] In this publication, we utilize ab initio molecular dynamics to assess the effect of water on the vibrational properties. Several reactions in the atmosphere occur in the presence of water, which may have rather substantial implications on rates and branching ratios in many instances. The catalytic effects of organic reactions occurring on a water surface have been shown to increase rate constants by stabilizing reaction intermediates through the enhanced availability of hydrogen bonding on the surface of water droplets.[25] High stereo- and regioselectivity has also been observed with on-water reactions.[25] Implications on atmospheric reaction rates and branching ratios are apparent. Stratospheric ice, for example, catalyzes the reaction of HCl and $ClONO_2$ to form Cl_2 and HNO_3.[26] Another example, relevant to tropospheric chemistry, is that the decomposition of a isoprene ozonolysis product has been theoretically shown to have enhanced reaction rates in the presence of a single water molecule.[27] [The calculations in ref 27, however, involve harmonic analysis of hydrogen-bonded intermediates, which has a restricted influence as we will show in this paper (and as already noted in refs 9−14).] In a review concerning tropospheric ozone, Jacob iterates the need for data concerning atmospheric aerosols and various reactive surfactants, such as hydroxyl peroxy radicals from isoprene oxidation.[28] Because the major interaction between aerosols and surfactants is through hydrogen bonding, it is useful to examine the behavior of the hydrogen-bonded atoms. Therefore, it is of interest to understand the interaction of the reactive species and intermediates, such as the hydroxyl peroxy-isoprene radical, and the water molecules that might result in the formation of an aerosol. Work presented in refs 6 and 9−15 indicates that hydrogen bonding affects both the vibrational density of states as well as vibrational energy redistribution and stabilization. In the case of hydroxyl peroxy-isoprene radicals on the surface of an atmospheric aerosol, this interaction will be predominantly comprised of the hydroxyl group hydrogen bonding to the adjacent waters in the aerosol. To probe the effect that this hydrogen bonding may have on the reactivity and stability of hydroxyl peroxy-isoprene, here we investigate the enthalpic and entropic stability of hydroxy-isoprene as well as the influence on its OH stretch and bend modes in the presence of water. Both electronic structure as well as AIMD simulations are used. Although the atmospheric fate of hydroxyl-isoprene alkyl radicals is predominately the reaction with O_2 to form peroxy radicals, understanding the influence of water on the stability and vibrational energy distribution of the OH-isoprene adducts is of interest theoretically. The results of this study will be useful to compare to studies of the impact of water on the stability and vibrational energy distribution of isoprene-based peroxy radicals, which will be a topic of a future publication.

In ref 11, Iyengar carried out AIMD and electronic structure studies on hydroperoxyl water clusters. It was found that (a) the thermally averaged electronic energy gap between the highest occupied molecular orbital and the lowest unoccupied molecular orbital monotonically decreases as the number of water molecules is increased in a hydroperoxyl water cluster system and (b) structural analysis from the dynamics simulation indicated that the oxygen−oxygen distance in a solvated hydroperoxyl−water cluster is very similar to that found in protonated water clusters (Zundel: $H_5O_2^+$) in spite of the fact that the latter possesses a positive charge and the hydroperoxyl−water cluster does not. Thus, strong "hydrogen-like" bonds may prevail in such systems, and these aspects are also noted for the hydroxy isoprene system studied here.

This paper is organized as follows: In section 2, the simulation strategies are described and the results are provided in sections 3 and 4. Specifically, in section 3 we probe (a) the stability of interactions between a cluster of water molecules (in the range of 1−15 water molecules) and a hydroxy-isoprene, adduct 1 molecule,[6] and (b) the influence on the vibrational density of states, computed within the harmonic approximation.

In section 4, we further investigate these results by including the effect of anharmonicity as available through potential energy sampling within an AIMD calculation. Conclusions are given in section 5.

2. THEORETICAL METHODS

The ab intio molecular dynamics (AIMD) simulations involve performing quantum chemical calculations "on-the-fly" to obtain the potential energy and nuclear forces.[29−38] The simulations conducted here are similar to those discussed in refs 6, 9−13,15, and 39. The atom-centered density matrix propagation (ADMP),[14,15,18,34,40−44] AIMD technique, as implemented within the Gaussian series of electronic structure codes,[45] has been employed in these studies. This method is briefly reviewed in Appendix A. Further details on the methodological aspects can be found in refs 34, 40−44 and 46 with applications in refs 6, 9−11, 14, 15, 18, 39, 41, 46, and 47.

All systems considered here are treated as gas-phase clusters to remain consistent with the experimental work.[6] A fictitious mass-tensor scaling value of 0.1 amu·bohr^2 (≈180 a.u.) and a time-step of 0.25 fs was used for ADMP. The AIMD simulations conducted here are microcanonical (NVE), with acceptable fluctuations in the internal temperature. All nuclei are treated classically. Because time-correlation functions involving nuclear velocities and molecular dipoles (see below) are utilized to obtain vibrational energy distributions, a constant energy simulation with an associated conservative Hamiltonian corresponding to the real system is critical. (These constant energy simulations however also have approximately fixed temperatures, with acceptable fluctuations.) The total energy in these simulations was well conserved in our simulations. The total angular momentum of the classical nuclear system was also well-conserved (with initial conditions corresponding to $J = 0$) and residual angular forces, resulting from finite numerical precision, were projected out during the dynamics process.[13] A body-fixed 3N-dimensional Cartesian coordinate system positioned at the center-of-mass, conserved all through the dynamics, was used to represent nuclear positions and momenta.

The dynamically averaged vibrational properties were computed by using Fourier-transform of the nuclear velocity auto-correlation function (FT-VAC):

$$\begin{aligned} I_{\mathrm{V}}(\omega) &= \lim_{T\to\infty}\int_{t=0}^{t=T} \mathrm{d}t\, \exp(-i\omega t)\langle \mathbf{V}(0)\cdot\mathbf{V}(t)\rangle \\ &= \lim_{T\to\infty}\sum_{i=1}^{N_{\mathrm{atoms}}}\sum_{j=1}^{3}\int_{t=0}^{t=T}\mathrm{d}t\, \exp(-i\omega t) \\ &\quad\times \int_{t'=0}^{t'=T}\mathrm{d}t' V_{i,j}(t')\, V_{i,j}(t'+t) \\ &= \lim_{T\to\infty}\sum_{i=1}^{N_{\mathrm{atoms}}}\sum_{j=1}^{3}\left|\int_{t=0}^{t=T}\mathrm{d}t\, \exp(-i\omega t) V_{i,j}(t)\right|^2 \end{aligned} \tag{4}$$

where the term $\langle\cdots\rangle$, in the first equation, indicates ensemble average and is equal to the t'-integral (enclosed within square-brackets) in the second equation under the ergodicity condition. The quantity $V_{i,j}(t)$ is the velocity along the j-th component for the i-th atom. We have used the convolution theorem[48] to reduce the second equation to the third equation. In Appendix B we also construct the quantum-mechanical analogue of eq 4, using the flux operator, and demostrate that vibrational states are obtained from such a formalism with intensities proportional to kinetic energy. See discussion below and also refs 6, 8−16, and 39.

During the dynamical process, the molecular structure evolves, which brings about a change in the electronic structure of the molecule and, hence, change in dipole of the system. The Fourier transform of the dipole−dipole autocorrelation function (FT-DAC) gives the IR spectrum for these clusters and is given by

$$\begin{aligned} \alpha_{\mu}^{\mathrm{QC}}(\omega) \propto \frac{\omega}{1-\exp(-\beta\hbar\omega)}\Big\{\omega[1-\exp(-\beta\hbar\omega)] \\ \times \lim_{T\to\infty}\int_{t=0}^{t=T}\mathrm{d}t\, \exp(-i\omega t)\langle \boldsymbol{\mu}(0)\cdot\boldsymbol{\mu}(t)\rangle\Big\} \end{aligned} \tag{5}$$

The terms inside the curly brackets ($\{\cdots\}$) represents the power normalized absorption cross-section.[49,50] The prefactor, $(\omega)/(1-\exp(-\beta\hbar\omega))$, is a quantum-nuclear correction[51−53] obtained based on the harmonic approximation. Utilizing the convolution theorem[48] as above, eq 5 may be rewritten as

$$\alpha_{\mu}^{\mathrm{QC}}(\omega) \propto \omega^2 \lim_{T\to\infty}\sum_{i=1}^{3}\left|\int_{t=0}^{t=T}\mathrm{d}t\, \exp(-i\omega t)\mu_i(t)\right|^2 \tag{6}$$

In this work, eq 4 is used to analyze vibrational energy density and eq 6 is used for comparison.

2.1. Tools for Analysis of Vibrational Energy Density. *2.1.1. Formal Analyses and Extensions Based on eq 4.* How does the above formalism relate to standard approaches for computing vibrational energy density? One of the most commonly used techniques to estimate vibrational density of states as well as to compute infrared spectra through ab initio electronic structure calculations invokes the harmonic approximation. Here a set of normal modes, $\{\vec{H}_i\}$, that are eigenstates of the mass-weighted Hessian matrix and force constants, $\{k_i\}$, that are eigenvalues of the mass-weighted Hessian are used to estimate the vibrational density of states. Other methods applicable to smaller gas-phase systems include full quantum nuclear or semiclassical treatment. The systems treated here, however, are large water clusters that range in size from 54 to 180 degrees of freedom, where full quantum nuclear treatment is prohibitive.

How can the velocity vectors introduced in eq 4 be related to the normal modes, $\{\vec{H}_i\}$? To understand this, we first introduce the mass-weighted velocity vector, $\mathcal{V}(t)$, with components

$$\mathcal{V}_{i,j}(t) \equiv \sqrt{M_i}V_{i,j}(t) \tag{7}$$

and the associated Fourier transform vector, $\tilde{\mathcal{V}}^{t'}(\omega,t)$, defined inside a given time-window, $[t,t']$, with components,

$$\tilde{\mathcal{V}}^{t'}_{j,k}(\omega,t) = \int_0^T \mathrm{d}t\, \exp[-i\omega t'']w(t'';t,t')\mathcal{V}_{j,k}(t'') \tag{8}$$

Here, $w(t'';t,t')$ is a suitably chosen window function. Windowed Fourier transforms or short-time Fourier transforms[54−57] are used to construct a local frequency analysis and determine the sinusoidal frequency and phase content of local sections of a signal as it changes over time. These have been previously used in chemical physics[58−60] and other areas[61] to study time-dependent behavior. For example, finite Fourier transforms have been used in ref 59 to derive new forms of the time-dependent Schrödinger equation. The associated time-frequency distribution is called a spectrogram and is used in our study to understand energy redistribution. In the studies presented here, $w(t'';t,t')$ has been

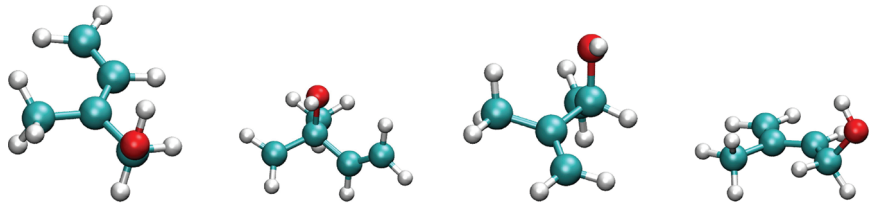

Figure 1. Optimized structures for the four hydroxy isoprene adducts. Level of theory: B3LYP/6-311++G(D,P).

chosen as a step function that is equal to one inside $[t,t']$ and zero otherwise. Choosing a time-window allows one to monitor the transient behavior. For example, the Fourier transform in eq 8 may be monitored as a function of t, for a given window $(t' - t)$. This is particularly critical to the analysis AIMD trajectories presented here. For fluxional systems, such as the water clusters treated here, the system may sample multiple regions of configurational space during a dynamics trajectory. As a result, eq 8 allows us to probe the periodic orbits of frequency ω that may be critical at time t. The time-dependence in the quantity, $\widetilde{\mathcal{V}}^{t'}(\omega,t)$, then probes how the critical frequency contributions vary as the system passes from one region in configurational space to another. We also note that when the window function in eq 8 is chosen to enclose the full time window, that is, $w(t'';t = 0, t' = T)$, the left-hand side becomes the usual Fourier transform of $\widetilde{\mathcal{V}}^{t'}(\omega,t)$. In that case, transient behavior is not present in eq 8, and we simplify the notation as $\widetilde{\mathcal{V}}_{t'=T}(\omega,t = 0) \equiv \widetilde{\mathcal{V}}(\omega)$.

If we now utilize the definitions in eqs 7 and 8, we may simplify eq 4 as

$$I_V(\omega) = \lim_{T\to\infty} \sum_{i=1}^{N_{atoms}} \frac{1}{M_i} \sum_{j=1}^{3} \left| \int_{t=0}^{t=T} dt \exp(-i\omega t)\, \mathcal{V}_{i,j}(t) \right|^2 = \sum_{i=1}^{N_{atoms}} \sum_{j=1}^{3} \frac{1}{M_i} |\widetilde{\mathcal{V}}_{i,j}(\omega)|^2 \quad (9)$$

or when the transient quantities are used:

$$I_V(\omega;t',t) = \sum_{i=1}^{N_{atoms}} \sum_{j=1}^{3} \frac{1}{M_i} |\widetilde{\mathcal{V}}^{t}_{i,j}(\omega,t)|^2 \quad (10)$$

Furthermore, the numerators on the right side of eqs 9 and 10 are mass-weighted velocities.

The physical interpretation for $I_V(\omega)$ is as follows. Integrating both sides of eq 9 with respect to ω and using Parsevaal's theorem,[48] one obtains

$$\begin{aligned} \frac{1}{T}\int d\omega I_V(\omega) &= \sum_{i=1}^{N_{atoms}} \sum_{j=1}^{3} \frac{1}{TM_i} \int d\omega |\widetilde{\mathcal{V}}_{i,j}(\omega)|^2 \\ &= \sum_{i=1}^{N_{atoms}} \sum_{j=1}^{3} \frac{1}{TM_i} \int dt |\mathcal{V}_{i,j}(t)|^2 \\ &= \sum_{i=1}^{N_{atoms}} \frac{1}{TM_i} \int dt [\sum_{j=1}^{3} |\mathcal{V}_{i,j}(t)|^2] \\ &= \sum_{i=1}^{N_{atoms}} \frac{1}{TM_i} \langle \mathcal{V}_i \cdot \mathcal{V}_i \rangle \\ &= 2 \sum_{i=1}^{N_{atoms}} \langle \mathcal{K}_i \rangle = 2\langle \mathcal{K} \rangle \end{aligned} \quad (11)$$

where $\mathcal{V}_i$ and $\mathcal{K}_i$ signify the velocity and kinetic energy for the i-th atom. The quantity $\mathcal{K}$ represents the total kinetic energy and $\langle \cdots \rangle$ is its ensemble averaged expectation value. Thus, the quantity $I_V(\omega)$ is proportional to a kinetic energy density at frequency ω or energy, $\hbar\omega$. Furthermore, using the Virial theorem[62,63] (where for a potential with polynomial dependence $V(x) = \alpha x^n$, the expectation values for potential and kinetic energies are related by $\langle \mathcal{K} \rangle = n\langle \mathcal{V} \rangle$), the right side of eq 11 is also proportional to the average potential energy of the system. Thus, $I_V(\omega)$ is also proportional to a potential energy density at frequency ω or energy, $\hbar\omega$. When $I_V(\omega)$ is normalized, it represents a density of kinetic energy (or potential energy) at frequency ω.

The quantity $I_V(\omega)$ has been used in several recent publications to compute the vibrational density of states.[6,9−16,39] In Appendix B, we present a formal analysis that derives the relations between the quantum density of states and the quantity $I_V(\omega)$.

2.1.2. Decomposition of $I_V(\omega;t',t)$ in Terms of a Complete Set of Vectors To Analyze Energy Redistribution. We next note that the normal mode vectors, $\{\vec{H}_i\}$, form a complete orthonormal set in 3N-space since these are eigenstates of a Hermitian Hessian matrix [In ref 13, the set $\{\vec{H}_i\}$ has also been found to be numerically complete during the dynamics in the 3N-6 internal space for a short-strong hydrogen-bonded system. Furthermore, while the discussion below assumes that $\{\vec{H}_i\}$ are eigenstates of the Hessian matrix, in fact, $\{\vec{H}_i\}$ can be any complete, orthonormal set of vectors about which the dynamics is to be inspected.] Because the vectors, $\widetilde{\mathcal{V}}(t)$ and $\widetilde{\mathcal{V}}^{t'}(\omega,t)$ also span the same $3N-6$ space we expand these in terms of the complete orthonormal set $\{\vec{H}_i\}$ as

$$\widetilde{\mathcal{V}}^{t'}(\omega,t) = \sum_i C_{i,t'}(\omega,t)\, \vec{H}_i \quad (12)$$

or

$$C_{i,t'}(\omega,t) = \widetilde{\mathcal{V}}^{t'}(\omega,t) \cdot \vec{H}_i \quad (13)$$

Using these equations in eq 10, one obtains

$$I_V(\omega;t',t) = \sum_{k,k'} C_{k,t'}(\omega,t)^* C_{k',t'}(\omega,t) \sum_{i=1}^{N_{atoms}} \sum_{j=1}^{3} \frac{H_k^{i,j}}{\sqrt{M_i}} \frac{H_{k'}^{i,j}}{\sqrt{M_i}} = \sum_k \frac{|C_{k,t'}(\omega,t)|^2}{\mu_k} \quad (14)$$

where $H_k^{ij}/(M_i)^{1/2}$ are elements of the orthonormal normal modes in Cartesian coordinates, with mass tensor μ_k. Thus, the quantity $|C_{k,t'}(\omega,t)|^2$ may be interpreted as the kinetic energy in the mode k at frequency ω in the time-window $[t,t']$. In this publication, we utilize this quantity to inspect the transient nature of vibrational density of states. In addition, we also probe the behavior of the same quantity in the full

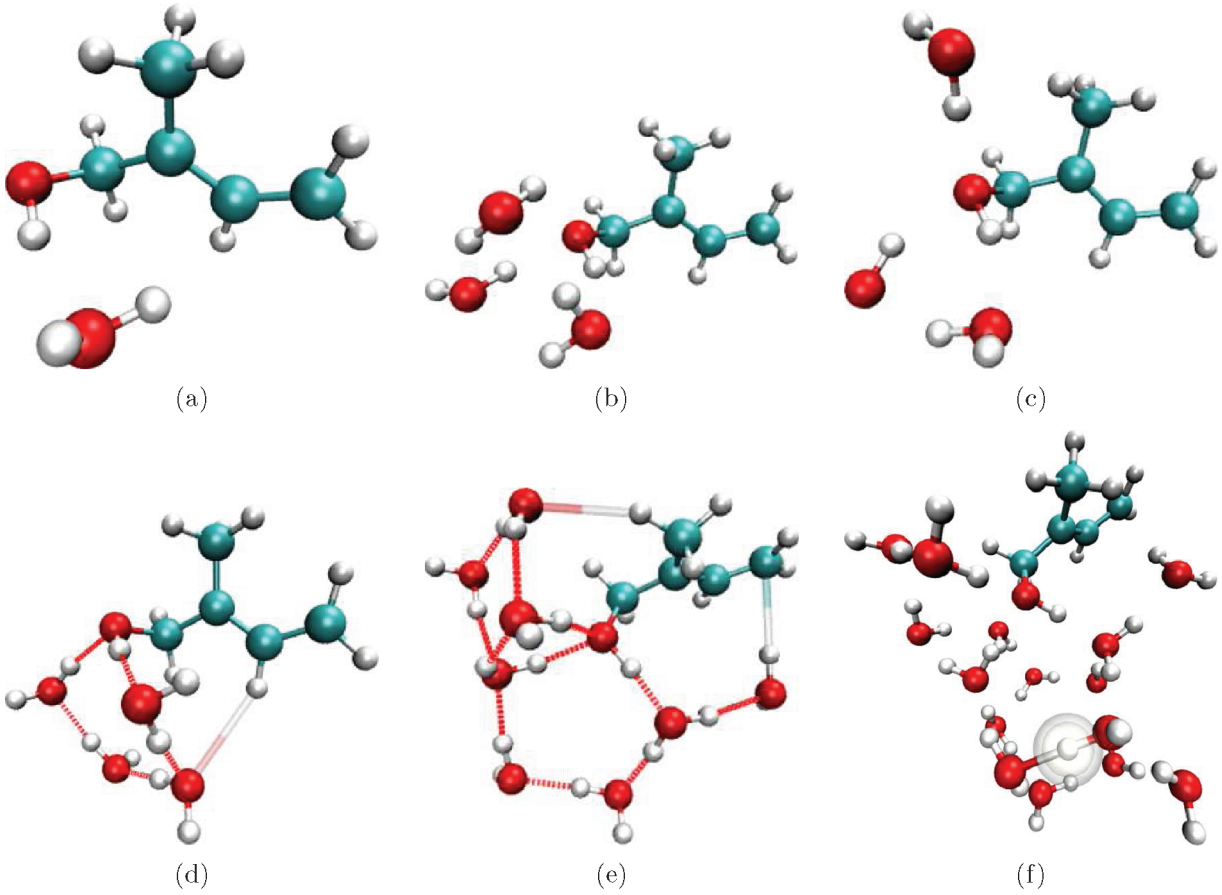

Figure 2. Geometries optimized to local minima of HO-isoprene·$(H_2O)_n$ clusters: 1 (a), 3 (b,c), 4 (d), 8 (e), and 15 (f) waters. All images are from B3LYP calculations except (c), which is from MP2. The minimum energy conformations for all clusters except the three-water cluster are similar for B3LYP amd MP2. In (d) and (e), dashed red lines indicate hydrogen bonding networks, while the faded lines represent water/alkyl hydrogen-like bonds. The hydrogen circled in (f) shows the most red-shifted OH stretch positioned across two water molecules. This occurrence is not possible in the smaller clusters where the most red-shifted OH stretch is the isoprene-hydroxyl stretch.

time window:

$$C_i(\omega) \equiv C_{i,t'=T}(\omega, t = 0) \tag{15}$$

It must be noted that this last quantity is identical to that used in refs 6, 12, 13, and 19. Specifically, eq 15 has been used in refs 12 and 13 to probe energy redistribution[64−76] in a short strong hydrogen bonded system. However, the derivation above also specifies a method to probe transient behavior. In addition, we note that while $\{\vec{H}_i\}$ are chosen to be harmonic normal mode vectors here, this is not a restriction and in principle these could specify any complete orthonormal set.

3. STRUCTURAL AND VIBRATIONAL PROPERTIES OF SOLVATED HYDROXY-ISOPRENE CLUSTERS WITHIN THE HARMONIC APPROXIMATION

The systems probed in the remaining portion of this study all include one hydroxy-isoprene molecule solvated by a water cluster. In this study, the role of water on the vibrational density of states of hydroxy-isoprene adduct 1 is considered. (The optimized geometry for all four adducts are shown in Figure 1.) For each of a set of clusters, properties of the HO-isoprene hydroxyl group were computed for optimized structures. These properties include vibrational frequencies, Mulliken charges, and cluster binding energies and were used to estimate a small cluster size with which to model the effects of an aerosol on the HO-isoprene. Ab initio dynamics trajectories were then computed for select clusters along with corresponding finite-temperature vibrational spectra (section 4), where dynamical averaging and anharmonicities significantly affect the vibrational properties.

The clusters included in this study range in size from 1−15 water molecules. To build these clusters, 1−3 water molecules were added at a time, between which the cluster structure was optimized. Geometry optimizations were performed using the basis set 6-31G(d). Higher order 6-31+G** basis functions were used to qualitatively confirm the results. Clusters with up to 15 waters were optimized with the spin unrestricted hybrid density functional, B3LYP. Second-order Möller-Plesset perturbation theory, MP2, was utilized for up to 8 waters.

The hydroxyl group on the HO-isoprene molecule will be affected by the introduction of additional water molecules. To probe the effect on the shared proton stretch, harmonic frequencies were computed for all optimized clusters. In addition, the charge separation between the oxygen and hydrogen of the hydroxyl group was calculated as the difference between the Mulliken charges on those two atoms. Finally, the binding energy was computed in two different ways. In one case the cluster binding energy for HO-isoprene·$(H_2O)_n$ was computed as

$$\Delta E_{\text{cluster}} = n \times E_{\text{water}} + E_{\text{HO-isoprene}} - E_{\text{cluster}} \tag{16}$$

dx.doi.org/10.1021/jp204511v |J. Phys. Chem. A 2012, 116, 399–414

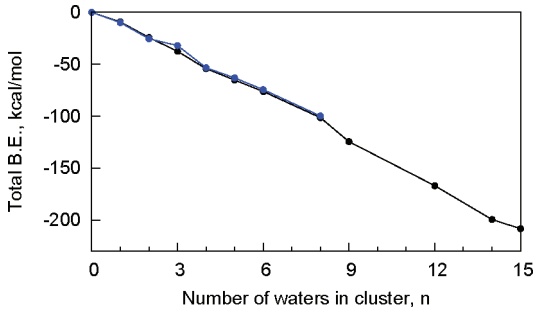

Figure 3. Stability of the interaction between hydroxy isoprene and water is indicated by the total binding energy ($\Delta E_{cluster}$ in eq 16) as a function of number of water molecules: black, B3LYP; blue, MP2. On average, 13 kcal/mol (amounting to about two hydrogen bonds) is gained in stability with the addition of each water molecule.

where E_{water} and $E_{HO-isoprene}$ are both optimized energies for a single water and hydroxy-isoprene, respectively. In a second approach the binding propensity of hydroxy-isoprene to water was gauged using

$$\Delta E = E_{n-\text{water}} + E_{\text{HO-isoprene}-f} - E_{\text{cluster}} \quad (17)$$

where $E_{n\text{-water}}$ is the energy of the n-water cluster retained at the same geometry as in the optimized HO-isoprene$\cdot(H_2O)_n$ cluster. Similarly, $E_{HO-isoprene-f}$ is also the energy of hydroxy-isoprene maintained at the same geometry as in the optimized HO-isoprene$\cdot(H_2O)_n$ cluster. In both cases, $E_{cluster}$ is the absolute energy of the optimized cluster.

3.1. Analysis of Optimized Cluster Geometries. Geometry optimizations to local minima were performed using B3LYP/6-31G(d). Cluster sizes studied range from 1−15 water molecules solvating a single hydroxy-isoprene molecule. The clusters with up to 8 water molecules were also optimized with MP2. Representative optimized geometries are provided in Figure 2. The DFT and MP2 geometries differed for the three water cluster and hence both structures are provided for this case (cf. Figure 2b,c). In both methods, the first two water molecules form a triangular geometry with the hydroxyl group. However, while the third water molecule formed hydrogen bonds with the hydroxyl group and the other waters in the DFT geometry, it formed only one hydrogen bond to the hydroxyl group and a weak interaction with a methyl hydrogen in the MP2 geometry. Clearly, the latter involves a dispersion interaction which is absent in B3LYP. For other cluster sizes, the optimized structures for the two methods are in good qualitative agreement.

As expected, a significant primary interaction between the water cluster and the hydroxy-isoprene radical is via hydrogen bonding to the hydroxyl group. However, there are a number of weak interactions influencing the geometry of the cluster as well. There are many instances of weak interactions between water oxygens and alkyl hydrogens (see Figures 2c−e) and the overall stable interaction between hydroxy isoprene and water is indicated by the total binding energy ($\Delta E_{cluster}$ in eq 16) shown in Figure 3. (Also see Table 1 for the dependence of $\Delta E_{cluster}$ on level of theory.) In Figure 3 we present $\Delta E_{cluster}$ obtained from both B3LYP, as well as MP2, for a variety of cluster sizes. The two levels of theory are generally in good agreement. (This may also be seen from Table 1.) Close inspection of Figure 3 indicates that the stabilization increases roughly linearly up to the point where eight water molecules are added; the stabilization energy per water grows faster beyond eight waters. The structure with eight water molecules in shown in Figure 2e where all the hydrogen bond locations in the first shell are saturated. On average it appears that two hydrogen bonds are formed as each new water molecule is added to the cluster. The most significant nonhydrogen bonding interaction, however, appears to be a hydrogen-bond-like interaction between one of the water hydrogens and the delocalized radical electron-cloud situated to the opposite end from the OH-group in hydroxy-isoprene molecule. This is a very consistent interaction for the set of optimized structures in this study, occurring in clusters with six or more waters. For cases with fewer than six water molecules, these are generally spatially well-separated from the oxygen end. For the case of one water, a hydrogen bond is formed with the hydroxyl group, but with no other waters present to interact with, the free hydrogen end of the water is directed toward the "hydrophobic" moiety. This is shown in Figure 2a. In the cases of six or more water molecules, the water hydrogen is pointing in the direction of the terminal carbon, suggesting that this is where the largest portion of negative charge resides. This is supported by a spin density analysis (see Figure 4) as well as Mulliken population analysis, which assigns the terminal carbon with the greatest negative charge among the three sp^2 carbons.

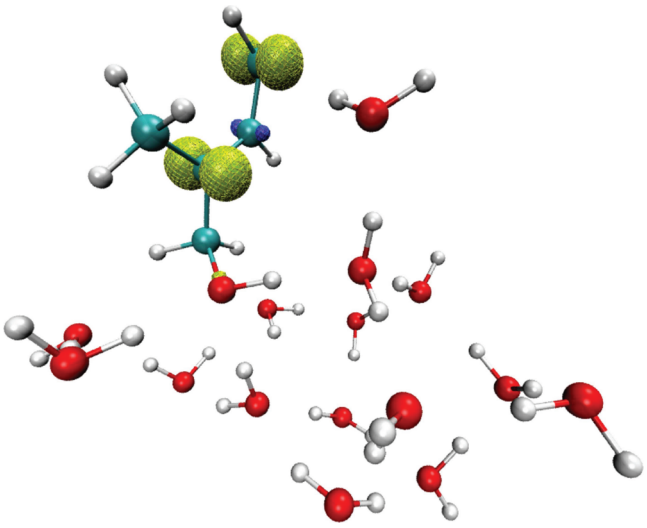

Figure 4. Spin density plot indicates that the free-radical remains localized on the 2- and 4-positions of hydroxy isoprene even in the presence of water. This remains the case for all water clusters studied here.

In general, the optimized geometries of these clusters are characterized by a few different interactions. Within the hydrogen bonding network of the water clusters, there is a prominence of five-membered rings. While five-membered rings comprising intramolecular hydrogen bond-like interactions were also noted for the case of hydroxy-isoprene adduct 1 in refs 6 and 19, the interactions here involve water, as can be noted from Figure 2d,e. Furthermore, these five-membered rings are reminiscent of similar topologies seen in hydroxyl water clusters,[10] lending some credence to the idea that solutes may enforce further order on the solvating water molecules. As for the interaction of the water cluster with the hydroxy-isoprene molecule, the most important is the hydrogen bonding to the hydroxyl group followed by weaker interactions to the radical end and alkyl hydrogens.

3.2. Harmonic Analysis of O−H Stretch in Optimized Structures. The harmonic frequencies are displayed in Figure 5.

Table 1. Dependence of the Total Binding Energy ($\Delta E_{cluster}$ in eq 16) on Level of Theory[a]

	B3LYP		MP2		CCSD(T)
	6-31G(D)	6-311++G(2D,2P)[b]	6-31G(D)	6-311++G(2D,2P)[c]	6-311++G(2D,2P)[d]
1[e]	−9.307	−5.077	−9.878	−7.436	−7.211
2[e]	−24.383	−14.838	−23.629	−16.897	−16.867
3[e]	−37.363	−26.047	−36.798	−25.098	−28.103
avg[f]	−11.842	−7.660	−11.718	−8.239	−8.697

[a] Units: kcal/mol. [b] b3lyp/6-311++g(2d,2p) geometries optimized starting from the b3lyp/6-31+g(d) optimized geometries. [c] mp2/6-311++g(2d,2p) geometries optimized from mp2/6-31+g(d) geometries, which in turn were optimized from b3lyp/6-31+g(d) optimized geometries. [d] ccsd(t)/6-311++g(2d,2p) single point calculations on mp2/6-311++g(2d,2p) geometries. [e] Number of water molecules. [f] Average stabilization energy per water molecule.

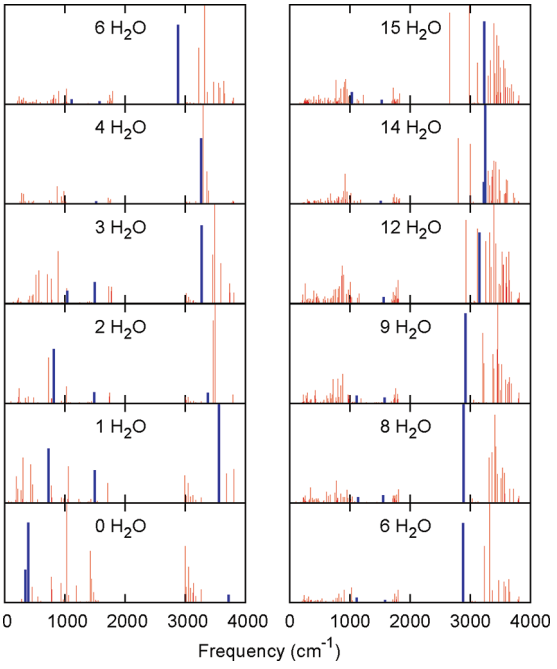

Figure 5. Harmonic frequencies for the HO-isoprene·$(H_2O)_n$ clusters. The peaks in blue represent the OH stretch (higher frequency) and bend (lower frequency) for hydroxy isoprene. These peaks clearly shift substantially as the number of water molecules is increased. See Figure 6.

It may be noted that, within the harmonic approximation, the modes that predominantly depict the isoprene-hydroxyl stretch and bend shift substantially as a result of hydration. For example, for the zero water case, the stretch and bend are very well separated (see the separation between the blue vertical lines in the bottom left panel of Figure 5). However, as water molecules are added, the separation reduces and the hydroxyl stretch begins to red-shift as a result of solvation. This appears to occur until the point where six water molecules surround the hydroxyl end of the isoprene molecule at which stage the trend begins to flatten out. Beyond nine water molecules, the hydroxyl stretch begins to blue shift again while the bending vibrations appear to have been stabilized near their six water value. (As we see later in section 4,

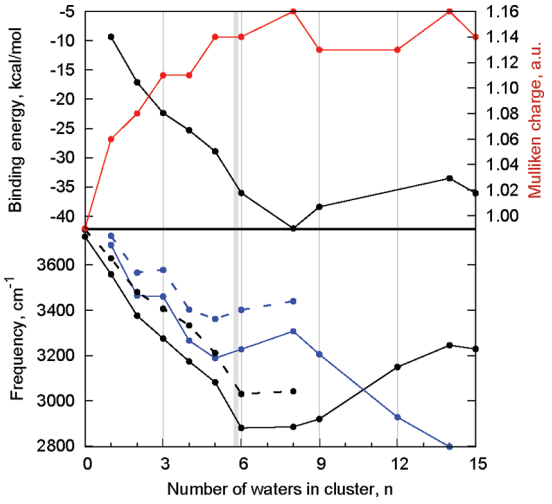

Figure 6. Trends from single-point calculations on the optimized HO-isoprene·$(water)_n$ clusters. HO-isoprene·$(water)_n$ binding energy, ΔE in eq 17 (top, black); Mulliken charge difference between the hydroxyl oxygen and hydrogen (top, red); hydroxyl O−H stretch frequency (bottom, black); and lowest water O−H stretch frequency (bottom, blue). The dashed lines represent MP2 results, the rest being UB3LYP.

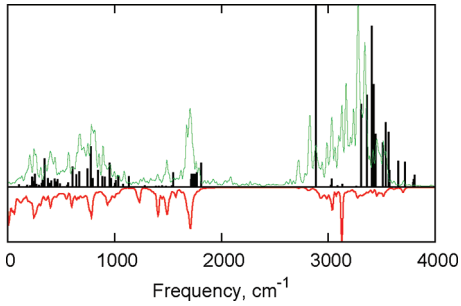

Figure 7. Vibrational spectra for the eight water cluster, including the harmonic IR frequency calculation (black), the velocity autocorrelation function (FT-VAC, eq 4; red), and the dipole autocorrelation function (FT-DAC, eq 5; green). The FT-VAC is shown along the negative vertical axis for clarity.

the hydroxyl stretch and bend modes are coupled when anharmonicity is included under finite temperature conditions.)

Due to hydrogen bonding, it is expected that the alcohol O−H stretch would be shifted when water is present as compared to the isolated HO-isoprene molecule. Initially, as the cluster size is increased, the alcohol O−H stretch was red-shifted by up to 800 cm^{-1} as in the case of the six water cluster. At the same time, water O−H stretches, which were at higher values, were red-shifted as well. After the sixth water, the red shift of the alcohol O−H stretch decreases with cluster size. After this point, water O−H stretches continued to be red-shifted and attain frequencies lower than the alcohol O−H stretch. These trends can be seen in the bottom panel of Figure 6. Two questions that emerge are (1) what caused the alcohol O−H stretch to stop being red-shifted at a cluster size of around six waters and (2) why did water O−H stretch frequencies trade places with the alcohol O−H stretch and attain the lower value in the larger cluster sizes?

To further probe the hydroxyl O−H stretch, the difference between the oxygen and hydrogen charges were calculated from a

dx.doi.org/10.1021/jp204511v |J. Phys. Chem. A 2012, 116, 399–414

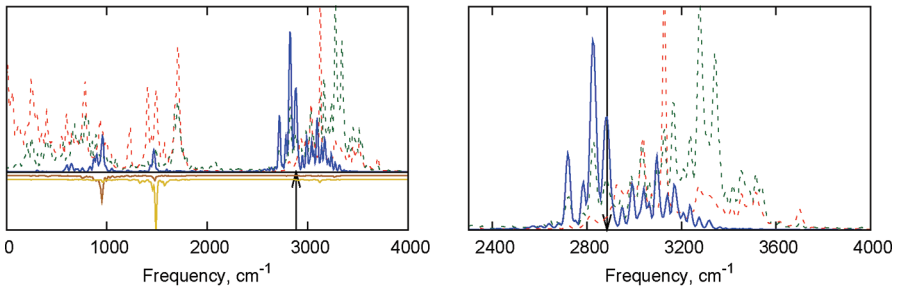

Figure 8. $[C_i(\omega)]^2$ (see eq 15) values from the hydroxy-isoprene O−H stretch mode contribution (blue) and O−H bend mode contributions (brown) are plotted on the negative vertical axis for clarity. (a) Full spectral range; (b), partial range. The plots indicate that the contributions from these Harmonic modes to the anharmonic dynamically averaged spectrum are delocalized over the entire spectral range. In addition, the FT-VAC (red) and the FT-DAC (green) are shown along the positive vertical axis for comparison. The arrow depicts the harmonic hydroxy-isoprene O−H stretch frequency at 2885 cm^{-1}. The harmonic bend modes can be found at ≈1500 and ≈1000 cm^{-1}. The blue curve indicates that, as a result of dynamics, the harmonic hydroxy-isoprene O−H stretch is coupled to the water stretch as well as the harmonic hydroxy-isoprene O−H bend modes.

Mulliken population analysis. While this may not provide a unique determination of the charges on the atoms, the general trend followed by the charge separation across the O−H bond may contain qualitative information about the change in bond strength. These charge differences, plotted in Figure 6 (red curve in the top panel), show that the introduction of water molecules increases the charge difference, weakening the bond, until the fifth water has been added, after which the charge difference stops increasing. This suggests that the hydrogen bonds of the first few waters weaken the O−H bond of the HO-isoprene hydroxyl group, thereby lowering its vibrational frequency, but as the first solvation shell becomes filled, further addition of water does not contribute to weakening the alcohol O−H bond. Because this reduction in Mulliken charge difference is associated with adding water molecules, we also see a complementary stabilization is indicated by ΔE (see eq 17), depicted by the black trace in the top panel of Figure 6. Both the Mulliken charge difference as well as ΔE appear to have been stabilized beyond six water molecules. [Compare the behavior of ΔE on the top panel of Figure 6 with that of $\Delta E_{cluster}$ (eq 16) in Figure 3. While ΔE estimates the binding interaction between hydroxy isoprene and the prearranged water cluster (see note following eq 17), $\Delta E_{cluster}$ estimates the total binding energy, including stability due to water−water interactions. Thus, ΔE represents the direct effect of water on hydroxy isoprene, and this effect tails off at roughly six water molecules.]

If increased hydrogen bonding results in a shift in the O−H stretch, then the addition of every water should shift the frequency. However, it is not that an increase in hydrogen bonding shifts the frequency, but rather that the increased bonding to the hydroxyl group results in a red shift. The ΔE binding energies in Figure 6, superimposed on the alcohol O−H stretch data, would ideally be energies of only the binding to the hydroxyl group (see discussion following eq 17), but since there is binding that occurs at other sites on the molecule, not all of the binding results in a shift of the O−H stretch. Still, the majority of the interaction between the water cluster and the HO-isoprene radical is through the hydrogen bonding to the alcohol group, so the trend in binding energy does turn out to predict at what approximate cluster size the O−H stretch will cease to be red-shifted. This will occur when further additional water molecules bind to only the water cluster and contribute no more binding to the molecule. At this point, the water cluster may be sufficiently large to model the local behavior of the HO-isoprene radical on the surface of a large aerosol droplet.

The analysis of the O−H charge difference and water cluster binding energies provide us with information about why the alcohol O−H frequency stops decreasing and at about which cluster size this occurs. Still, the question is left to answer, why, in the larger clusters, does a water O−H stretch trade places with the alcohol O−H stretch as having the lowest O−H stretch frequency value. To address this point, the cluster geometries described in the last section will be invoked. In the smaller clusters, the HO-isoprene hydroxyl group is the most coordinated of all O−H bonds, causing its frequency to be red-shifted more than any of the water O−H stretches. As can be seen in Figure 2f, when the cluster contains a sufficient number of water molecules, there may be water molecules in the system that are better coordinated than the alcohol group of HO-isoprene, causing the O−H stretch on a particular water to be the one whose frequency is shifted the most.

4. SPECTRAL ANALYSIS FROM AB INITIO MOLECULAR DYNAMICS

The ab initio molecular dynamics simulations were performed using atom-centered density matrix propagation (ADMP)[6,9−13,15,34,40−43,47] with B3LYP. The dynamics trajectories were NVE simulations carried out with time steps of 0.25 fs and an average temperature of 248 ± 28 K. The temperature is determined from the nuclear kinetic energy. This approach applies the equipartition theorem. It has been found in other studies using ADMP that this relation provides a good approximation to the cluster temperature.[10,12,13] Furthermore, as noted below, we utilize time-correlation functions constructuted using nuclear velocities. As a result, a dynamics trajectory that conserves the total energy is essential. Clusters containing six and eight waters were simulated up to approximately 5 ps of dynamics. These two clusters were chosen since they exhibited the largest shift in alcohol O−H stretching frequency, as indicated by the discussion in the previous section. In this study, the spectroscopic analysis of the eight water cluster will be explored.

The dipole spectrum (eq 6) and the vibrational density of states (eq 4) are presented in Figure 7 along with the harmonic stick spectrum. The harmonic and dipole spectra (black and green, respectively, in the upper panel) show qualitative agreement below 2000 cm^{-1}. In the higher frequency range the most

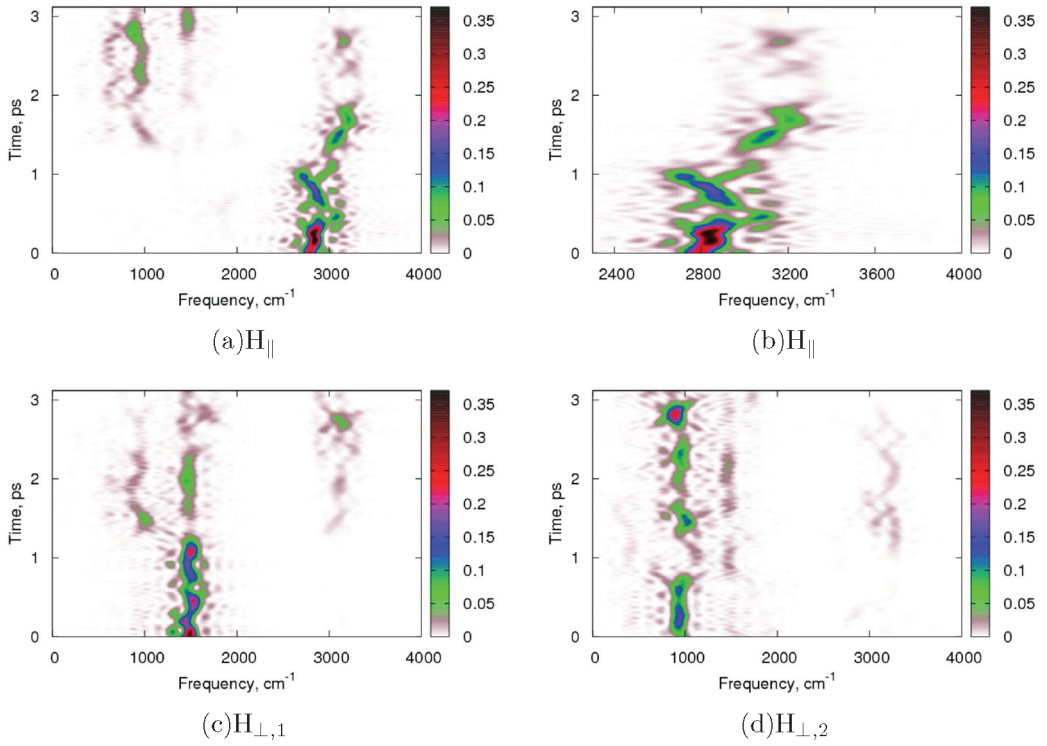

Figure 9. Time-frequency $|C_{i,t'}(\omega,t)|^2$ (see eq 13) analysis for hydroxy-isoprene O−H stretch mode contribution (a and b) and hydroxy-isoprene O−H bend contribution (c and d) underline the fluxional nature of these hydrogen-bonded systems.

prominent peak in the harmonic stick spectrum appears red-shifted (≈2885 cm^{-1}) with respect to the corresponding peaks in the dynamically averaged spectra. In the harmonic spectrum, this well-isolated peak with the greatest intensity is the isoprene−OH stretch mode located at 2885 cm^{-1}. The dipole spectrum does not contain such a prominent, well-separated peak. Rather than a well-pronounced peak in the dipole spectrum, there is only a small shoulder on the red-shifted water stretching band in the vicinity of the shared proton stretch of the harmonic spectrum. The question remains as to where exactly the isoprene−OH stretch appears in the dynamically averaged spectral result.

The apparent loss of intensity from the shared proton stretch prevents its straightforward identification (see also refs 9−11 for similar shifts in frequencies in water clusters). To gauge this effect, we provide the quantity $|C_i(\omega)|^2$ (see eq 15) for the hydroxy-isoprene OH stretch (blue) and the two orthogonal bends (brown) in Figure 8a. The quantity $|C_i(\omega)|^2$ provides a measure of the contribution from harmonic mode i (which in this case is the mode that is predominantly an isoprene−OH stretch or bend) to the dynamically averaged spectral intensity at frequency ω. While the most prominent stretch contribution still appears close to its harmonic fundamental (black arrow in Figure 8a), the contributions from the stretch shown are clearly delocalized as a result of dynamical averaging and thermal sampling of the potential surface. Specifically, the isoprene−OH stretch couples, as expected, into the water−OH stretch spectral region (>3000 cm^{-1}) as well as its own bend. This dynamical mixing of the harmonic fundamental OH stretch is quite similar to that encountered in refs 9−11 and 13 where again the shared proton stretch in a hydrogen-bonded system was found to contribute almost over the entire spectral range when finite-temperature

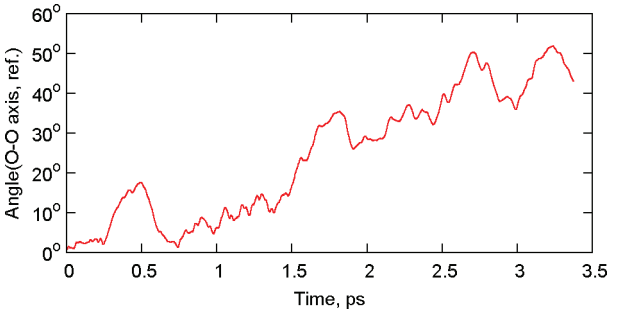

Figure 10. The time evolution of the polar angle between the shared proton O−O axis and the O−O axis in the reference equilibrium structure upon which the harmonic normal coordinates are defined.

dynamical averaging was taken into account. However, what is also interesting to note in Figure 8 is the fact that the isoprene−OH stretch provides significant contributions at the 1000 and 1500 cm^{-1} regions, which are expected to be predominantly bend-dominated regions.

To further gauge the effect seen in Figure 8, we inspect the time-dependent evolution of contributions from the harmonic stretch and bend modes emanating from the HO-isoprene moeity. This is seen from an analysis of $|C_{i,t'}(\omega,t)|^2$ (see eq 13), as depicted in the spectrograms in Figure 9. Specifically, in Figure 9a,b we provide contributions arising from the harmonic stretch to the dynamically averaged (FT-VAC) spectrum. That is, in Figure 9a,b, we depict $|C_{i,t'}(\omega,t)|^2$, for $i = H_{||}$, as noted in the subfigure caption. These figures again underline the effect seen in Figure 8 where contributions arise from the spectral region greater than 3000 cm^{-1} as well as the lower frequency region.

dx.doi.org/10.1021/jp204511v |J. Phys. Chem. A 2012, 116, 399–414

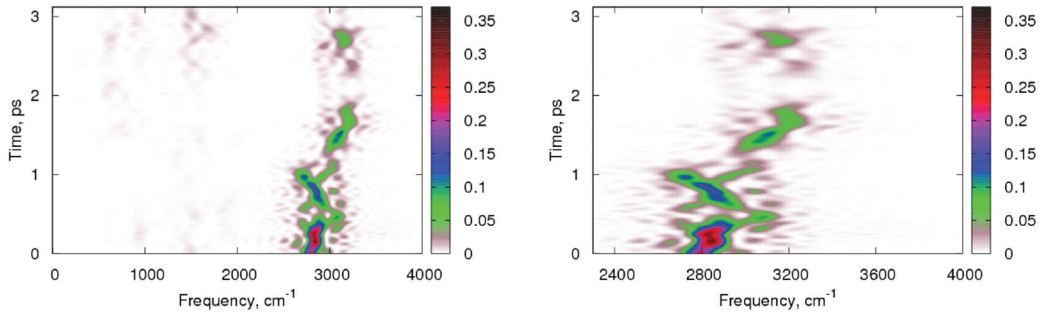

Figure 11. Time-frequency evolution of $|\tilde{C}^{OO}_{H_{\|},H_{\perp;t'}}(\omega,t)|^2$ (see eq 18).

Figure 9, however, also provides a temporal resolution that is absent in Figure 8.

In Figure 9c,d, we provide contributions arising from the harmonic bend modes. While the fundamental harmonic stretch appears at 2885 cm^{-1}, the bend appears at around 1000 and 1500 cm^{-1}. However, these are all coupled as a result of dynamics and it is this effect that is captured through the cumulative blue and brown traces in Figure 8.

The analysis above indicates that the hydroxy OH stretch and bend modes that appear pure within the harmonic approximation are now coupled as a result of anharmonicity as it is introduced in the analysis through the ab initio dynamics calculations.

We next probe the reasons behind such a coupled feature. While the total angular momentum is well conserved within the dynamics calculation, there exists a change in OH bond orientation during dynamics, as indicated in Figure 10, and provides a vehicle to couple the harmonic bend and stretch modes. We may project out such an internal rotation-induced coupling in the spectrum by computing the evolution of

$$\begin{aligned}\tilde{C}^{OO}_{H_{\|},H_{\perp;t'}}(\omega,t) \equiv\ & [(\tilde{\mathscr{V}}^{t'}(\omega,t)\cdot \vec{H}_{i=H_{\|}})\,\vec{H}_{i=H_{\|}} \\ & + (\tilde{\mathscr{V}}^{t'}(\omega,t)\cdot \vec{H}_{i=H_{\perp,1}})\,\vec{H}_{i=H_{\perp,1}} \\ & + (\tilde{\mathscr{V}}^{t'}(\omega,t)\cdot \vec{H}_{i=H_{\perp,2}})\,\vec{H}_{i=H_{\perp,2}}]\cdot\hat{R}_{OO}(t) \\ =\ & [C_{i=H_{\|},t'}(\omega,t)\,\vec{H}_{i=H_{\|}} + C_{i=H_{\perp,1},t'}(\omega,t)\,\vec{H}_{i=H_{\perp,1}} \\ & + C_{i=H_{\perp,2},t'}(\omega,t)\,\vec{H}_{i=H_{\perp,2}}]\cdot\hat{R}_{OO}(t) \qquad (18)\end{aligned}$$

where we have defined the new quantity $\tilde{C}^{OO}_{H_{\|},H_{\perp;t'}}(\omega,t)$ in terms of $C_{i,t'}(\omega,t)$ introduced in eq 13. Essentially, $\tilde{C}^{OO}_{H_{\|},H_{\perp;t'}}(\omega,t)$ is the projection of the spectral components in Figure 9 along the instantaneous OO axis. The corresponding time-frequency evolution of $\tilde{C}^{OO}_{H_{\|},H_{\perp;t'}}(\omega,t)$ is shown in Figure 11. In comparing Figures 11 and 9a, it is clear that, while Figure 9a shows contributions from the bend modes toward the FT-VAC spectrum, this is not the case in Figure 11. *Clearly internal rotation of the OH bond has the effect of coupling these modes thus providing an additional degree of freedom for energy redistribution that is absent within the harmonic approximation, but is present in the dynamics calculations and facilitated by sampling of the anharmonic potential surface.*

5. CONCLUSION

In this manuscipt, ab initio molecular dynamics and static electronic structure calculations are utilized to assess the influence of water on the stability and vibrational density of states of a hydroxy-isoprene adduct. This is done to model the effect of atmospheric water on a radical intermediate relevant to atmospheric chemistry. As expected, the most prominent interactions between the water clusters and the hydroxy-isoprene adduct are through hydrogen bonding to the alcohol group. Of the nonhydrogen bonding interactions was an attraction between water hydrogen atoms and the radical electron delocalized across the carbons opposite of the alcohol group. The radical interacted consistently with clusters of six or more waters; for all cluster sizes, the hydroxy-isoprene radical was found on the surface of the water cluster.

Vibrational frequency calculations within the harmonic model showed that addition of water molecules resulted in a red-shift of the hydroxy-isoprene OH stretch, the red-shift being nearly linear with cluster size up to the six water cluster in which the maximum shift, of 800 cm^{-1}, occurred. Mulliken charge analysis showed that as more water molecules were introduced the charge difference between the alcohol oxygen and hydrogen widened, indicating a weakening of the bond as the alcohol group interacts with the water cluster. The widening of the charge difference as well as the water cluster/hydroxy-isoprene binding energy stabilize also at the six water cluster. These trends support the use of clusters with as few as six water molecules to model the influence of atmospheric aerosol adsorption of the hydroxy-isoprene radical.

The ab initio molecular dynamics of hydroxy-isoprene on a cluster of eight water molecules were used to compute time-averaged and transient time dependent vibrational spectra. In the static harmonic model calculation, the vibrational frequency of the alcohol OH stretch corresponded to a peak in the simulated IR spectrum that was the largest in intensity and well isolated at 2885 cm^{-1}. In contrast, the spectrum computed from the dynamics trajectory produced no large, well-separated peak in that region, but merely a shoulder on a broad water OH stretching band. The vibrational density of states projected along the alcohol OH stretch harmonic normal coordinate indicated that the peak was well dispersed over a wide frequency range from 2700 to 3300 cm^{-1} as well as contributing to peaks at 1000 and 1500 cm^{-1} where the alcohol bending frequencies were expected to be found. The source of the coupling between the harmonic stretching and bending modes were probed using a computational technique, introduced here: two-dimensional spectra representing transient vibrational densities of states were computed along the harmonic normal modes. It was found that a local, internal, rotation caused the observed coupling of the vibrational modes, rotating the alcohol OH axis by up to 50°.

The internal rotation present in the dynamics trajectory allows for additional pathways of intramolecular vibrational energy redistribution.

APPENDIX A

Brief Overview of the Theoretical Basis for the Extended Lagrangian Ab Initio Molecular Dynamics Method, Atom-Centered Density Matrix Propagation (ADMP). The method of ab initio molecular dynamics (AIMD) relies on a calculation of the electronic potential energy surface traversed by the nuclei "on-the-fly" during the dynamics procedure. Both Born-Oppenheimer (BO) molecular dynamics (MD),[29−36,77] as well as Car-Parrinello (CP) dynamics,[32,35,77−79] are part of this category. The CP scheme differs from the BO dynamics approach in that the wavefunctions are propagated together with the classical nuclear degrees of freedom using an extended Lagrangian. This, in turn, relies on an adjustment of the relative nuclear and electronic time-scales, which facilitates the adiabatic propagation of the electronic wavefunction in response to the nuclear motion with suitably large time steps. This adjustment of time scales through the use of a fictitious electronic wavefunction kinetic energy and mass, enables the CP approach to predict effectively similar nuclear dynamics on the BO surface at significantly reduced cost. In this respect, CP differs from methods which rigorously treat the detailed dynamics (rather than structure) of the electrons (see ref 33 and references therein). The CP method is essentially an extended Lagrangian[80,81] dynamics scheme in which the electronic degrees of freedom are not iterated to convergence at each step, but are instead treated as fictitious dynamical variables and propagated along with the nuclear degrees of freedom by a simple adjustment of time scales. The resultant energy surface remains close to a converged adiabatic electronic surface. Numerous important examples of applications with density functional theory and the CP method are now well documented in the literature (see, e.g., ref 35 and 78). In the original CP approach, the KohnSham molecular orbitals, expanded in a plane-wave basis, were chosen as dynamical variables to represent the electronic degrees of freedom.[77] However, this is not the only possible choice. An alternative approach is to propagate the individual elements of the reduced one-particle density matrix, **P**.

In atom-centered density matrix propagation (ADMP),[34,40−44,46] atom-centered Gaussian basis sets are employed to represent the single-particle electronic density matrix within an extended Lagrangian formalism. Here, the basis functions follow the nuclei. The ADMP method has several attractive features. Systems can be simulated by accurately treating all electrons or by using pseudo-potentials. Through the use of smaller values for the tensorial fictitious mass, relatively large time steps can be employed and lighter atoms such as hydrogens are routinely used. A wide variety of exchange-correlation functionals can be utilized, including hybrid density functionals such as B3LYP. Atom-centered functions can be used with the appropriate physical boundary conditions for molecules, polymers, surfaces, and solids, without the need to treat replicated images to impose 3d periodicity. This is particularly relevant to atmospheric clusters that are described here. A QM/MM generalization has been demonstrated.[46] ADMP has been demonstrated through the treatment of several interesting problems, including[6,9,11−15,39,41,43,46] (a) a recent demonstration that dynamical effects are critical in obtaining good vibrational spectroscopic properties of flexible systems[9−13,39] and (b) the prediction of the "amphiphilic" nature of the hydrated proton,[15,39,82] which has now been confirmed by many experimental and theoretical studies.

The ADMP equations of motion for the nuclei and density matrix are derived from the extended Lagrangian:

$$\mathcal{L} = \frac{1}{2}\mathbf{Tr}[\mathbf{V}^{\mathbf{T}}\mathbf{M}\mathbf{V}] + \frac{1}{2}\mathbf{Tr}[(\underline{\mu}^{1/4}\mathbf{W}\underline{\mu}^{1/4})^2] - E(\mathbf{R}_C, \mathbf{P}, R_{QM}) - \mathbf{Tr}[\Lambda(\mathbf{P}^2 - \mathbf{P})] \quad (A1)$$

where **R**, **V**, and **M** are the nuclear positions, velocities, and masses and **P**, **W**, and $\underline{\mu}$ are the density matrix, the density matrix velocity, and the fictitious mass tensor for the electronic degrees of freedom. Λ is a Lagrangian multiplier matrix used to impose N-representability of the single particle density matrix. The energy, E(R,P), is calculated using McWeeny purification, $\tilde{\mathbf{P}} = 3\mathbf{P}^2 - 2\mathbf{P}^3$,

$$E = \mathrm{Tr}\left[\mathbf{h}'\tilde{\mathbf{P}}' + \frac{1}{2}\mathbf{G}'(\tilde{\mathbf{P}}')\tilde{\mathbf{P}}'\right] + E_{xc} + V_{NN} = \mathrm{Tr}\left[\mathbf{h}\tilde{\mathbf{P}} + \frac{1}{2}\mathbf{G}(\tilde{\mathbf{P}})\tilde{\mathbf{P}}\right] + E_{xc} + V_{NN} \quad (A2)$$

Here, $\mathbf{h}'$ is the one electron matrix in the nonorthogonal Gaussian basis and $\mathbf{G}'(\tilde{\mathbf{P}}')$ is the two electron matrix for Hartree-Fock calculations, but for DFT it represents the Coulomb potential. The term E_{xc} is the DFT exchange-correlation functional (for Hartree-Fock $E_{xc} = 0$), while V_{NN} represents the nuclear repulsion energy. In the orthonormal basis, these matrices are $\mathbf{h} = \mathbf{U}^{-\mathbf{T}}\mathbf{h}'\mathbf{U}^{-1}$, and so on, where the overlap matrix for the nonorthogonal Gaussian basis, $\mathbf{S}'$, is factorized to yield $\mathbf{S}' = \mathbf{U}^{\mathbf{T}}\mathbf{U}$. There are a number of choices for the transformation matrix **U**, for example, **U** can be obtained from Cholesky decomposition[83] of $\mathbf{S}'$ or $\mathbf{U} = \mathbf{S}'^{1/2}$ for Löwdin symmetric orthogonalization. The matrix **U** can also include an additional transformation so that overall rotation of the system is factored out of the propagation of the density. The density matrix in the orthonormal basis, **P**, is related to the density matrix in the nonorthogonal Gaussian basis, $\mathbf{P}'$, by $\mathbf{P} \equiv \mathbf{U}\mathbf{P}'\mathbf{U}^{\mathbf{T}}$.

The equations of motion for the above formalism are

$$\mathbf{M}\frac{\mathrm{d}^2\mathbf{R}}{\mathrm{d}t^2} = -\left.\frac{\partial E(\mathbf{R},\mathbf{P})}{\partial \mathbf{R}}\right|_{\mathbf{P}} \quad (A3)$$

$$\underline{\mu}^{1/2}\frac{\mathrm{d}^2\mathbf{P}}{\mathrm{d}t^2}\underline{\mu}^{1/2} = -\left[\left.\frac{\partial E(\mathbf{R},\mathbf{P})}{\partial \mathbf{P}}\right|_{\mathbf{R}} + \Lambda\mathbf{P} + \mathbf{P}\Lambda - \Lambda\right] \quad (A4)$$

These equations are numerically integrated using the velocity Verlet scheme.[40,84] The gradient terms involved in the equations of motion are

$$\left.\frac{\partial E(\mathbf{R},\mathbf{P})}{\partial \mathbf{P}}\right|_{\mathbf{R}} = 3\mathbf{F}\mathbf{P} + 3\mathbf{P}\mathbf{F} - 2\mathbf{F}\mathbf{P}^2 - 2\mathbf{P}\mathbf{F}\mathbf{P} - 2\mathbf{P}^2\mathbf{F} \quad (A5)$$

where **F** is the Fock matrix and in the nonorthogonal basis:

$$\mathbf{F}'_{\nu,\sigma} \equiv \mathbf{h}'_{\nu,\sigma} + \mathbf{G}'(\tilde{\mathbf{P}}')_{\nu,\sigma} + \frac{\partial E_{xc}}{\partial \mathbf{P}'} \quad (A6)$$

dx.doi.org/10.1021/jp204511v |J. Phys. Chem. A 2012, 116, 399–414

while the orthogonal basis Fock matrix is $\mathbf{F} = \mathbf{U}^{-\mathrm{T}}\mathbf{F}'\mathbf{U}^{-1}$. The nuclear gradients are

$$\left.\frac{\partial E}{\partial \mathbf{R}}\right|_{\mathrm{P}} = \left\{ \mathrm{Tr}\left[\frac{\mathrm{d}\mathbf{h}'}{\mathrm{d}\mathbf{R}}\tilde{\mathbf{P}}' + \frac{1}{2}\left.\frac{\partial \mathbf{G}'(\mathbf{P}')}{\partial \mathbf{R}}\right|_{\mathrm{P}'}\tilde{\mathbf{P}}'\right] - \mathrm{Tr}\left[\mathbf{F}'\tilde{\mathbf{P}}'\frac{\mathrm{d}\mathbf{S}'}{\mathrm{d}\mathbf{R}}\tilde{\mathbf{P}}'\right] + \left.\frac{\partial E_{\mathrm{xc}}}{\partial \mathbf{R}}\right|_{\mathrm{P}} + \frac{\partial V_{\mathrm{NN}}}{\partial \mathbf{R}}\right\} + \mathrm{Tr}\left[[\tilde{\mathbf{P}}, \mathbf{F}]\left(\tilde{\mathbf{Q}}\frac{\mathrm{dU}}{\mathrm{dR}}\mathbf{U}^{-1} - \tilde{\mathbf{P}}\mathbf{U}^{-\mathrm{T}}\frac{\mathrm{dU}^{\mathrm{T}}}{\mathrm{dR}}\right)\right] \tag{A7}$$

where $\tilde{\mathbf{Q}} \equiv \mathbf{I} - \tilde{\mathbf{P}}$. It has been shown that,[40,42] as the commutator $[\tilde{\mathbf{P}},\mathbf{F}] \rightarrow 0$, the nuclear forces tend toward those used in the standard Born-Oppenheimer MD.[85] However, in ADMP, the magnitude of the commutator $[\tilde{\mathbf{P}},\mathbf{F}]$ is non-negligible, and hence, the general expression for the nuclear gradients[34,42] in eq A7 is used.

Because the conjugate Hamiltonian was derived from a Legendre transform[63] of the Lagrangian in eq A1:

$$\mathscr{H}(\mathbf{P}, \mathscr{W}, \mathbf{R}, \mathscr{V}, t) = \mathrm{Tr}(\mathscr{W}\mathbf{W}) + \mathrm{Tr}(\mathscr{V}^{\mathrm{T}}\mathbf{V}) - \mathscr{L}(\mathbf{P}, \mathbf{W}, \mathbf{R}, \mathbf{V}, t) \tag{A8}$$

where $\mathscr{W}$ and $\mathscr{V}$ are the conjugate momenta for $\mathbf{P}$ and $\mathbf{R}$, respectively, and are given by

$$\mathscr{W} = \frac{\partial \mathscr{L}}{\partial \mathbf{W}} = \underline{\mu}^{1/2}\mathbf{W}\underline{\mu}^{1/2} \tag{A9}$$

and

$$\mathscr{V} = \frac{\partial \mathscr{L}}{\partial \mathbf{V}} = \mathbf{M}\mathbf{V} \tag{A10}$$

is conservative, that is,

$$\frac{\mathrm{d}\mathscr{H}}{\mathrm{d}t} = 0 \tag{A11}$$

the integrated velocity Verlet equations obtained from eqs A3 and A4 conserve the total energy to within the micro-hartree range for time steps of the order of 0.25 fs. Because the velocity Verlet equations are obtained from a third order[44] Trotter factorization[86,87] of the Liouville equation for eqs A3 and A4,[44] the integration error grows as the third power of the chosen dynamics time step. Hence, angular momentum is also well-conserved within the numerical limits enforced by the third order integration scheme. It must, however, be emphasized that this simulation scheme is purely classical from the point of view of the nuclei. One of the deficiencies of such an approach is the restricted zero-point constraint.[88−90] The problem of constraining classical dynamics equations through the influence of the zero-point vibrational modes which in turn include the full anharmonic potential surface is a challenging and unsolved problem in chemical physics. Common approaches[88−90] include constraining the dynamics using modes obtained through a local harmonic approximation. Our approach here does not include these effects.

Like CP, ADMP represents fictitious dynamics where the density matrix is propagated instead of being converged. The accuracy and efficiency is governed by the choice of the fictitious mass tensor, $\underline{\mu}$; hence, one must be aware of the limits on this quantity. We have derived two independent criteria[40,42] that place bounds on the choice of the fictitious mass. Firstly, the choice of the fictitious mass determines the magnitude of the commutator $[\tilde{\mathbf{P}},\mathbf{F}]$, thus, determining the extent of deviation from the Born-Oppenheimer surface:[42]

$$||[\mathbf{F}, \mathbf{P}_{\mathrm{approx}}]||_F \geq \frac{1}{||[\mathbf{P}_{\mathrm{approx}}, \mathbf{W}]||_F}\left|\mathrm{Tr}\left[\mathbf{W}\underline{\mu}^{1/2}\frac{\mathrm{d}\mathbf{W}}{\mathrm{d}t}\underline{\mu}^{1/2}\right]\right| \tag{A12}$$

where $||[...]||_F$ is the Frobenius norm[83,91] of the commutator and is defined as $||A||_F = (\Sigma_{i,j}A_{i,j}^{\ 2})^{1/2}$. Secondly, the rate of change of the fictitious kinetic energy,

$$\frac{\mathrm{d}\mathscr{H}_{\mathrm{fict}}}{\mathrm{d}t} = \mathrm{Tr}\left[\mathbf{W}\underline{\mu}^{1/2}\frac{\mathrm{d}^2\mathbf{P}}{\mathrm{d}t^2}\underline{\mu}^{1/2}\right] = -\mathrm{Tr}\left[\mathbf{W}\left(\left.\frac{\partial E(\mathbf{R}, \mathbf{P})}{\partial \mathrm{P}}\right|_{\mathrm{R}} + \mathbf{\Lambda}\mathbf{P} + \mathbf{P}\mathbf{\Lambda} - \mathbf{\Lambda}\right)\right] \tag{A13}$$

is to be bounded and oscillatory and this again is determined by the choice of fictitious mass tensor. We have shown that ADMP gives results that are in good agreement with BOMD and is computationally superior to BOMD.[41] However, one must monitor the quantities in eqs A12 and A13 to ascertain that the ADMP dynamics is physically consistent. In all applications studied to date,[9,11,15,34,39−41,46] these conditions are satisfied, thus, yielding a computationally efficient and accurate approach to model dynamics on the Born-Oppenheimer surface.

Current implementation of the ADMP approach has been found to be computationally superior to Born-Oppenheimer dynamics.[41] This important result can be conceptualized based on the following: In Born Oppenheimer dynamics, the density matrix is to be converged at every dynamics step. Assuming that the largest possible time step is used during dynamics, SCF convergence requires approximately 8−12 SCF steps (this depends on the convergence threshold and difficult cases such as transition metal complexes may require more SCF steps). In ADMP, on the contrary, only the equivalent of 1 SCF step is required per dynamics step; this 1 SCF step is necessary to calculate the Fock matrix required for propagating the density matrix. (A brief review of ADMP is presented in Section A.) Both BOMD and ADMP evaluate the gradient of energy with respect to nuclear coordinates, and this calculation requires approximately the same amount of time in both methods. Note that the gradients used in ADMP are more general than those used in BOMD[34,42] on account of the non-negligible magnitude of the commutator of the Fock and density matrix (see Section A and ref 42 for details). However, the additional terms require no significant computation over the standard BOMD gradient calculation. The calculation of nuclear force requires approximately 3 times as much computation time as a single SCF cycle. This makes ADMP faster than BOMD by over a factor of 4 per dynamics step. However, the requirement that the ADMP energies oscillate about the BO values with small amplitudes[40] implies that ADMP step sizes cannot be as large at those in BO dynamics. But good energy conservation, which applies to both methods, limits the BO steps to at most twice those of ADMP[41] (ADMP already uses reasonably large time-steps on account of smaller values for the fictitious mass and an innovative tensorial fictitious mass scheme[40]). This allows ADMP to be over a factor of 2 superior to BOMD, but this estimate is only for cases where the SCF convergence in BOMD is not difficult.[41] The hard to converge cases would require more SCF steps (or a better SCF

convergence algorithm), thus, making ADMP more efficient as compared to BOMD for these cases. Furthermore, computational improvements that speed up the gradient evaluation will tilt this comparison further towards ADMP.

1. Treatment of Anharmonic Hydrogen-Bonded Systems Using Ab Initio Molecular Dynamics: Case Study for the Highly Anharmponic Cl−H−Cl$^-$ Moiety. As indicated earlier, the dynamics techniques used here have been employed to treat many hydrogen-bonded systems. See, for example, ref 6, 8−16, and 39. In this section, a brief case-study is presented for the Cl−H−Cl$^-$ system. Data from ref 80 is excerpted here in Tables 2 and 3, for convenience. The first block of data in Table 2 depicts harmonic frequencies obtained from electronic structure calculations as well as excitation energies obtained using potential surfaces for the shared proton for frozen Cl−Cl distances. The second block shows experimental data provided from the velocity modulation spectroscopy[93,94] work in ref 92. As indicated by the first block of data, the harmonic approximation is inadequate at all levels of electronic structure theory. The proton potential energy surfaces shown in Figure 12 are obtained from retaining the Cl atoms at their respective optimized positions. A direct polynomial fit of these surfaces displays significant contributions from fourth and sixth order terms which explains the limited accuracy of the harmonic frequency calculations. In fact, borrowing the diatomic molecular spectroscopy notation,[95] the anharmonic constant $w_e x_e$, for ν_3 is a large negative number (see the last column of Table 2) as the spacing between the vibrational levels increases as opposed to that in the harmonic approximation. In Table 2, we also provide corrections to the harmonic approximation by computing three-dimensional proton eigenstate transition energies at the equilibrium Cl−Cl geometries for the respective levels of theory (see footnote e in Table 2). Even these calculations only provide an upper bound to the experimental results, though they significantly improve over the harmonic results. Clearly, in addition to anharmonicity, coupling between the proton and chloride motions is critical and is missing in the first block of data provided in Table 2.

In Table 3, we present our results from ab initio dynamics studies at constant energy (NVE) where spectra are computed using $I_V(\omega)$ in eq 4. De-convolving the FT-VAC spectra through analysis of the individual nuclear motions indicate temperature-dependent peaks corresponding to ν_1, ν_2, and ν_3. The dynamical spectra show an improvement in the ν_1 and ν_2 stretches over the harmonic approximation. The most dramatic change, however, is shown in the asymmetric proton stretch, ν_3. Most importantly, unlike the harmonic results, the ab initio dynamics studies are less sensitive to the electronic structure treatment as a result of dynamical averaging of the potential surface. Furthermore, the fact that ν_3 from the dynamics simulations are blue-shifted as compared to those from the harmonic approximation, underlines the importance of fourth order anharmonic contributions to the potential in this system.

The agreement with experiment is drastically improved when quantum nuclear effects are introduced in ab initio dynamics studies as done with the QWAIMD method.[8,37,96−100] See second block of Table 3. As can be seen the agreement between the QWAIMD results and experiment improves with increasing temperature. Due to a dependence of ν_3 on the simulation temperature, it is important to note that the experiments in ref 92 were performed using velocity modulation spectroscopy where the effective vibrational temperature could be as high as 1000K.[93,94] Hence, it is not surprising that the higher temperature QWAIMD results get closer to the experimental result. The reason why QWAIMD exhibits a temperature dependence in its vibrational properties is because as the temperature increases, the Cl−Cl geometry samples larger distances. Since the electronic

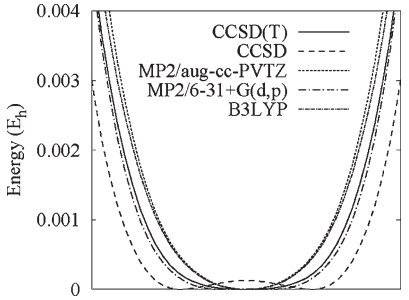

Figure 12. Displayed here are one-dimensional slices of the potential energy surfaces of the shared proton along the Cl−Cl axis at equilibrium geometries obtained at the levels of theory indicated in Table 2. The horizontal axis represents a spread of 0.529 Å (1 Bohr). The B3LYP/aug-cc-PVTZ and B3LYP/6-31+G(d,p) surfaces are indistinguishable and the CCSD surface shows a double well. The basis set used for both CCSD and CCSD(T) is aug-cc-PVTZ, as listed in Table 2.

Table 2. Vibrational Frequencies of Cl−H−Cl$^-$, As Computed Using Standard Methods[a]

level of theory	ν_1 (cm^{-1})	ν_2 (cm^{-1})		ν_3 (cm^{-1})		Cl−Cl dist. (Å)[b]	w_e (cm^{-1})[c]	$w_e x_e$ (cm^{-1})[c]
B3LYP/6-31+G(d,p)	328	834[d]	849[e]	560[d]	949[e]	3.15	827.54	−173.484
B3LYP/aug-cc-PVTZ	324	818[d]	829[e]	582[d]	952[e]	3.15	833.463	−169.508
MP2/6-31+G(d,p)	353	893[d]	907[e]	98[d]	865[e]	3.10	698.037	−217.648
MP2/aug-cc-PVTZ	345	847[d]	863[e]	637[d]	974[e]	3.11	858.043	−181.427
CCSD/aug-cc-PVTZ	181	828[d]	874[e]	833[d]	764[e]	3.14[f]	565.65	−228.137
CCSD(T)/aug-cc-PVTZ	340	842[d]		325[d]		3.12	730.253	−204.83
experiment[g]	318	792 ± 9		723				

[a] Anharmonic contributions are critical for ν_3, the shared proton stretch. The first block of data includes direct use of electronic structure methods within the harmonic approximation which appears to be inadequate for describing the anhmaronic shared proton stretch. In the last block experimental data is provided. [b] The Cl−Cl distance is computed at the optimized geometry obtained at the listed level of electronic structure theory. [c] Potential energy surface harmonic and anharmonic constants. [d] Harmonic frequency corresponding to the optimized geometry. [e] From three-dimensional 1 ← 0 eigenstate transitions. The potential energy surface for the eigenstates is obtained from a full-scan of the quantum proton, with the chlorides fixed at optimized geometry positions. Hence, the eigenstates here are corrected for anharmonicity, but do not include coupling with the chloride motions. [f] For CCSD, the shared proton is *not* symmetrically placed along the Cl−Cl axis. This is in contrast with respect to all other optimized geometries here. [g] Ref 92.

Table 3. Dynamically Averaged Vibrational Density of States Calculated from Classical Ab Initio Dynamics Studies[a]

level of theory	temp (K)[b]	ν_1 (cm^{-1})	ν_2 (cm^{-1})	ν_3 (cm^{-1})
B3LYP/6-31+G(d,p)	15.95	319	830	600
B3LYP/6-31+G(d,p)	50.29	308	818	658
B3LYP/6-31+G(d,p)	75.5	308	814	658
B3LYP/aug-cc-PVTZ	15.89	317	813	622
B3LYP/aug-cc-PVTZ	49.63	313	808	625
B3LYP/aug-cc-PVTZ	74.97	308	806	647
MP2/aug-cc-PVTZ	15.72	336	842	645
MP2/aug-cc-PVTZ	49.64	330	834	653
QWAIMD:B3LYP/6-31+G**	323.50	300	857	806
QWAIMD:B3LYP/6-31+G**	714.45	254	863	723
experiment[c]		318	792 ± 9	723

[a] Data excerpted from ref 8. [b] Average internal temperature of the system during the simulation computed using nuclear velocities. [c] Ref 92.

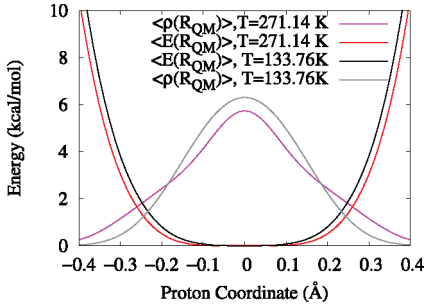

Figure 13. Temperature dependence of vibrational properties in QWAIMD. The system studied is Cl−H−Cl$^-$ as in Table 2.

potential surface adapts to this change within QWAIMD, this effectively flattens out the potential energy surface on the shared proton along the Cl−Cl distance at larger temperatures. Compare the higher temperature potential depicted using the red curve in Figure 13 with the corresponding lower temperature black curve. This reduced confinement on the shared proton lowers the transition energies as the wavepackets exhibit a broader distribution at higher temperatures. Compare the gray and magenta wavepacket curves in Figure 13. These lower transition energies for the higher temperature QWAIMD calculation are seen as a red-shift in the ν_3 transition frequency.

APPENDIX B

Vibrational Density of States and the Velocity Autocorrelation Function: Correspondence through the "Averaged" Quantum Flux Operator. In this section we further analyze $I_V(\omega)$ in eq 4 and its connections to the vibrational density of states.

The spectral density operator, $\delta(E-\mathbf{H})$,[59] provides a spectral decomposition of the Hamiltonian, $\mathbf{H}$ because the state $\delta(E-\mathbf{H})|\chi\rangle$ is always an eigenstate of $\mathbf{H}$, with eigenvalue E. In cases where E is not an eigenvalue, the state $\delta(E-\mathbf{H})|\chi\rangle$ is identically zero. This can be seen from the fact that $(E-\mathbf{H})\delta(E-\mathbf{H})|\chi\rangle = 0$ for all values of E. As a result, $\delta(E-\mathbf{H})$ provides a density of states for the Hamiltonian, $\mathbf{H}$.

We next examine the connections between the vibrational density of states and $I_V(\omega)$ in eq 4. Let us first define the quantum analogue of velocity as the expectation value or the "averaged" value of the flux operator:

$$\mathbf{J}(t) = \mathscr{R}\left[\left\langle \psi(t)\left|\frac{\hat{p}}{m}\right|\psi(t)\right\rangle\right] = \mathscr{R}\left[\left\langle \psi(t)\left|\frac{-i\hbar}{m}\nabla\right|\psi(t)\right\rangle\right]$$
$$= \mathscr{R}\left[\left\langle \psi(0)\exp(i\mathbf{H}t/\hbar)\left|\frac{-i\hbar}{m}\nabla\right|\exp(-i\mathbf{H}t/\hbar)\psi(0)\right\rangle\right] \quad \text{(B1)}$$

where the quantity $\mathscr{R}[\cdots]$ is the real part of the complex number within square brackets, and we have used the fact that $\psi(t) \equiv \exp(-i\mathbf{H}t/h)\psi(0)$. A spectral decomposition of the function $\psi(0)$, in terms of the eigenvalues and eigenstates of $\mathbf{H}$: $\{E_i,\phi_i\}$, then yields

$$\mathbf{J}(t) = \mathscr{R}\left[\left\langle \sum_i c_i\phi_i \exp\left\{\frac{iE_it}{\hbar}\right\}\left|\frac{-i\hbar}{m}\nabla\right|\sum_j \exp\left\{\frac{-iE_jt}{\hbar}\right\}c_j\phi_j\right\rangle\right]$$
$$= \mathscr{R}\left[\sum_{i,j}\frac{-i\hbar}{m}c_i^*c_j\exp\left\{\frac{i(E_i-E_j)t}{\hbar}\right\}\langle\phi_i|\nabla|\phi_j\rangle\right] \quad \text{(B2)}$$

Thus, the quantum analogue of the nuclear velocity autocorrelation function, $I_V(\omega)$ in eq 4, may be defined as the expectation value of flux autocorrelation function:

$$I_J(\omega) \equiv \int_{-\infty}^{+\infty} dt\, \exp[-i\omega t]\langle \mathbf{J}(t)\mathbf{J}(0)\rangle$$
$$\equiv \left|\int_{-\infty}^{+\infty} dt\, \exp[-i\omega t]\mathbf{J}(t)\right|^2 \quad \text{(B3)}$$

where we have used the convolution theorem[48] as in eq 4. Using eq B2, we obtain

$$I_J(\omega)$$
$$= \left|\int_{-\infty}^{+\infty} dt\, \exp\left[-i\omega t\right]\left\{\mathscr{R}\left[\sum_{i,j} c_i^*c_j\ \exp\left\{\frac{i(E_i-E_j)t}{\hbar}\right\}\frac{\langle\phi_i|\hat{\mathbf{P}}|\phi_j\rangle}{m}\right]\right\}\right|^2$$
$$= \left|\sum_{i,j}\delta\left(\omega-\frac{[E_i-E_j]}{\hbar}\right)c_i^*c_j\frac{\langle\phi_i|\hat{\mathbf{P}}|\phi_j\rangle}{m}\right.$$
$$\left.+\,\delta\left(\omega-\frac{[E_j-E_i]}{\hbar}\right)c_ic_j^*\frac{\langle\phi_i|\hat{\mathbf{P}}|\phi_j\rangle^*}{m}\right|^2 \quad \text{(B4)}$$

where $\delta(...)$ is the Dirac delta function. Equation B4 clearly leads to a spectral representation with peaks positioned at the various energy differences that correspond to vibrational excitations. This is due to the presence of the quantity $\delta(\omega-([E_j-E_i])/\hbar)$. However, unlike $\delta(E-\mathbf{H})$ above, $I_J(\omega)$ has peak intensities that are related to the velocity squared. (Note that kinetic energy is obtained in eq 11 when mass-weighted velocities are used.) Indeed, both the classical analogue of eq B3, that is $I_V(\omega)$ in eq 4, as well as $I_J(\omega)$ itself has been used in recent publications to perform a spectral decomposition. See, for example, ref 8 for the use of $I_J(\omega)$ to compute vibrational states and refs 6, 9−16, and 39 for the use of $I_V(\omega)$ in computing vibrational states.

AUTHOR INFORMATION

Corresponding Author
*E-mail: iyengar@indiana.edu.

■ ACKNOWLEDGMENT

This research is supported by the National Science Foundation Grant NSF CHE-1058949 to S.S.I. and the Indiana University research support Grant No. 2324701/NTBEE to S.S.I. Authors S.M.D. and A.B.P. thank Drs. Isaiah Sumner and Xiaohu Li for valuable discussions.

■ REFERENCES

(1) Sillman, S. *Annu. Rev. Energy Env.* **1993**, *18* (1), 31–56.
(2) Heard, D. E.; Pilling, M. J. *Chem. Rev.* **2003**, *103* (12), 5163–5198.
(3) Tan, D.; Faloona, I.; Simpas, J. B.; Brune, W.; Shepson, P. B.; Couch, T. L.; Sumner, A. L.; Carroll, M. A.; Thornberry, T.; Apel, E.; Riemer, D.; Stockwell, W. *J. Geophys. Res., [Atmos.]* **2001**, *106*, 24407–24427.
(4) Carslaw, N.; Creasey, D. J.; Harrison, D.; Heard, D. E.; Hunter, M. C.; Jacobs, P. J.; Jenkin, M. E.; Lee, J. D.; Lewis, A. C.; Pilling, M. J.; Saunders, S. M.; Seakins, P. W. *Atmos. Environ.* **2001**, *35*, 4725–4737.
(5) Guenther, A. *Nature* **2008**, *452* (7188), 701.
(6) Vimal, D.; Pacheco, A. B.; Iyengar, S. S.; Stevens, P. S. *J. Phys. Chem. A* **2008**, *112*, 7227.
(7) Peeters, J.; Nguyen, T. L.; Vereecken, L. *Phys. Chem. Chem. Phys.* **2009**, *11* (28), 5935–5939.
(8) Sumner, I.; Iyengar, S. S. *J. Phys. Chem. A* **2007**, *111*, 10313–10324.
(9) Iyengar, S. S. *J. Chem. Phys.* **2007**, *126*, 216101.
(10) Li, X.; Teige, V. E.; Iyengar, S. S. *J. Phys. Chem. A* **2007**, *111*, 4815–4820.
(11) Iyengar, S. S. *J. Chem. Phys.* **2005**, *123*, 084310.
(12) Li, X.; Moore, D. T.; Iyengar, S. S. *J. Chem. Phys.* **2008**, *128*, 184308.
(13) Li, X.; Oomens, J.; Eyler, J. R.; Moore, D. T.; Iyengar, S. S. *J. Chem. Phys.* **2010**, *132*, 244301.
(14) Iyengar, S. S.; Li, X.; Sumner, I. *Adv. Quantum Chem.* **2008**, *55*, 333–353.
(15) Iyengar, S. S.; Day, T. J. F.; Voth, G. A. *Int. J. Mass Spectrom.* **2005**, *241*, 197–204.
(16) Diken, E. G.; Headrick, J. M.; Roscioli, J. R.; Bopp, J. C.; Johnson, M. A.; McCoy, A. B. *J. Phys. Chem. A* **2005**, *109*, 1487–1490.
(17) Iyengar, S. S.; Sumner, I.; Jakowski, J. *J. Phys. Chem. B* **2008**, *112*, 7601.
(18) Iyengar, S. S. *Int. J. Quantum Chem.* **2009**, *109*, 3798.
(19) Pacheco, A. B.; Dietrick, S. M.; Stevens, P. S.; Iyengar, S. S. *J. Phys. Chem. A* **2011**, submitted for publication.
(20) Aloisio, S.; Francisco, J. S. *Acc. Chem. Res.* **2000**, *33*, 825–830.
(21) Aloisio, S.; Francisco, J. S. *J. Phys. Chem. A* **1998**, *102*, 1899–1902.
(22) Shi, Q.; Belair, S. D.; Francisco, J. S.; Kais, S. *Proc. Natl. Acad. Sci. U.S.A.* **2003**, *100* (17), 9686–9690.
(23) Clark, J.; Call, S. T.; Austin, D. E.; Hansen, J. C. *J. Phys. Chem. A* **2010**, *114*, 6534–6541.
(24) Vaida, V. *J. Chem. Phys.* **2011**, *109*, 020901.
(25) Jung, Y.; Marcus, R. A. *J. Am. Chem. Soc.* **2007**, *129*, 5492.
(26) Mantz, Y.; Geiger, F. M.; Molina, L. T.; Molina, M. J.; Trout, B. L. *J. Phys. Chem. A* **2001**, *105*, 7037.
(27) Aplincourt, P.; Anglada, J. M. *J. Phys. Chem. A* **2003**, *107*, 5812.
(28) Jacob, D. *Atmos. Environ.* **2000**, *34*, 2131.
(29) Wang, I. S. Y.; Karplus, M. *J. Am. Chem. Soc.* **1973**, *95*, 8160.
(30) Leforestier, C. *J. Chem. Phys.* **1978**, *68*, 4406.
(31) Bolton, K.; Hase, W. L.; Peslherbe, G. H. *Direct Dynamics of Reactive Systems*; World Scientific: Singapore, 1998; p 143.
(32) Payne, M. C.; Teter, M. P.; Allan, D. C.; Arias, T. A.; Joannopoulos, J. D. *Rev. Mod. Phys.* **1992**, *64*, 1045.
(33) Deumens, E.; Diz, A.; Longo, R.; Öhrn, Y. *Rev. Mod. Phys.* **1994**, *66*, 917.
(34) Schlegel, H. B.; Millam, J. M.; Iyengar, S. S.; Voth, G. A.; Daniels, A. D.; Scuseria, G. E.; Frisch, M. J. *J. Chem. Phys.* **2001**, *114*, 9758.
(35) Marx, D.; Hutter, J. *Ab Initio Molecular Dynamics: Theory and Implementation*; John von Neumann Institute for Computing: Julich, 2000; Vol. 1, pp 301−449.
(36) Schlegel, H. B. *J. Comput. Chem.* **2003**, *24*, 1514–1527.
(37) Iyengar, S. S.; Jakowski, J. *J. Chem. Phys.* **2005**, *122*, 114105.
(38) Martinez, T. J.; Ben-Nun, M.; Ashkenazi, G. *J. Chem. Phys.* **1996**, *104*, 2847.
(39) Iyengar, S. S.; Petersen, M. K.; Day, T. J. F.; Burnham, C. J.; Teige, V. E.; Voth, G. A. *J. Chem. Phys.* **2005**, *123*, 084309.
(40) Iyengar, S. S.; Schlegel, H. B.; Millam, J. M.; Voth, G. A.; Scuseria, G. E.; Frisch, M. J. *J. Chem. Phys.* **2001**, *115*, 10291.
(41) Schlegel, H. B.; Iyengar, S. S.; Li, X.; Millam, J. M.; Voth, G. A.; Scuseria, G. E.; Frisch, M. J. *J. Chem. Phys.* **2002**, *117*, 8694.
(42) Iyengar, S. S.; Schlegel, H. B.; Voth, G. A.; Millam, J. M.; Scuseria, G. E.; Frisch, M. J. *Isr. J. Chem.* **2002**, *42*, 191–202.
(43) Iyengar, S. S.; Frisch, M. J. *J. Chem. Phys.* **2004**, *121*, 5061.
(44) Iyengar, S. S.; Schlegel, H. B.; Voth, G. A. *J. Phys. Chem. A.* **2003**, *107*, 7269–7277.
(45) Frisch, M. J.; Trucks, G. W.; Schlegel, H. B.; Scuseria, G. E.; Robb, M. A.; Cheeseman, J. R.; Montgomery, J. A., Jr.; Vreven, T.; Kudin, K. N.; Burant, J. C.; Millam, J. M.; Iyengar, S. S.; Tomasi, J.; Barone, V.; Mennucci, B.; Cossi, M.; Scalmani, G.; Rega, N.; Petersson, G. A.; Nakatsuji, H.; Hada, M.; Ehara, M.; Toyota, K.; Fukuda, R.; Hasegawa, J.; Ishida, M.; Nakajima, T.; Honda, Y.; Kitao, O.; Nakai, H.; Klene, M.; Li, X.; Knox, J. E.; Hratchian, H. P.; Cross, J. B.; Adamo, C.; Jaramillo, J.; Gomperts, R.; Stratmann, R. E.; Yazyev, O.; Austin, A. J.; Cammi, R.; Pomelli, C.; Ochterski, J. W.; Ayala, P. Y.; Morokuma, K.; Voth, G. A.; Salvador, P.; Dannenberg, J. J.; Zakrzewski, V. G.; Dapprich, S.; Daniels, A. D.; Strain, M. C.; Farkas, O.; Malick, D. K.; Rabuck, A. D.; Raghavachari, K.; Foresman, J. B.; Ortiz, J. V.; Cui, Q.; Baboul, A. G.; Clifford, S.; Cioslowski, J.; Stefanov, B. B.; Liu, G.; Liashenko, A.; Piskorz, P.; Komaromi, I.; Martin, R. L.; Fox, D. J.; Keith, T.; Al-Laham, M. A.; Peng, C. Y.; Nanayakkara, A.; Challacombe, M.; Gill, P. M. W.; Johnson, B.; Chen, W.; Wong, M. W.; Gonzalez, C.; .; Pople, J. A. *Gaussian 03*, Revision B.02; Gaussian, Inc.: Pittsburgh, PA, 2003.
(46) Rega, N.; Iyengar, S. S.; Voth, G. A.; Schlegel, H. B.; Vreven, T.; Frisch, M. J. *J. Phys. Chem. B* **2004**, *108*, 4210–4220.
(47) Pavone, M.; Biczysko, M.; Rega, N.; Barone, V. *J. Phys. Chem. A* **2010**, *114*, 11509.
(48) Press, W. H.; Teukolsky, S. A.; Vetterling, W. T.; Flannery, B. P. *Numerical Recipes In C*; Cambridge University Press: New York, 1992.
(49) Gordon, R. G. *Adv. Magn. Reson.* **1968**, *3*, 1.
(50) McQuarrie, D. A. *Statistical Mechanics*; University Science Books: Sausalito, CA, 2000.
(51) Berens, P. H.; White, S. R.; Wilson, K. R. *J. Chem. Phys.* **1981**, *75*, 515.
(52) Bader, J. S.; Berne, B. J. *J. Chem. Phys.* **1994**, *100*, 8359.
(53) Lawrence, C. P.; Nakayama, A.; Makri, N.; Skinner, J. L. *J. Chem. Phys.* **2004**, *120*, 6621.
(54) Grocheng, K. *Constr. Approx.* **1993**, *9*, 283–297.
(55) Jacobsen, E.; Lyons, R. *Signal Process. Mag., IEEE* **2003**, *20*, 74–80.
(56) He, T. *J. Math. Anal. Appl.* **1998**, *224* (2), 182–200.
(57) Tolimieri, R.; An, M.; Lu, C. *Mathematics Of Multidimensional Fourier Transform Algorithms*; Springer-Verlag: New York, 1993.
(58) Martens, C. C.; Ezra, G. S. *J. Chem. Phys.* **1985**, *83*, 2990–3001.
(59) Iyengar, S. S.; Kouri, D. J.; Hoffman, D. K. *Theor. Chem. Acc.* **2000**, *104*, 471.
(60) Akama, T.; Nakai, H. *J. Chem. Phys.* **2010**, *132* (5), 054104.
(61) Hyvarinen, A.; Ramkumar, P.; Parkkonen, L.; Hari, R. *Neuroimage* **2010**, *49*, 257–271.
(62) Cohen-Tannoudji, C.; Diu, B.; Loloë, F. *Quantum Mechanics*; John Wiley And Sons: New York, 1977; Vol. II.
(63) Goldstein, H. *Classical Mechanics*; Addison Wesley: Boston, MA, 1980.
(64) Fermi, E.; Pasta, J. R.; Ulam, S. Studies of nonlinear problems. i. *Technical Report No. 1940*, Los Alamos Report, 1955.

(65) Robinson, P. J.; Holbrook, K. A. *Unimolecular Reactions*; Wiley: New York, 1972.
(66) Forst, W. *Theory of Unimolecular Reactions*; Academic Press: New York, 1973.
(67) Jortner, J.; Levine, R. *Adv. Chem. Phys.* **1981**, *47* (Part 1), 1.
(68) Parmenter, C. S. *J. Phys. Chem.* **1982**, *86*, 1735.
(69) Parmenter, C. S. *Faraday Discuss.* **1983**, *75*, 7.
(70) E. L. Sibert, I.; Reinhardt, W.; Hynes, J. *J. Chem. Phys.* **1984**, *82*, 1115.
(71) Khundkar, L. R.; Zewail, A. H. *Annu. Rev. Phys. Chem.* **1990**, *41*, 15.
(72) Uzer, T.; Miller, W. H. *Phys. Rep.* **1991**, *199*, 74.
(73) Nesbitt, D. J.; Field, R. W. *J. Chem. Phys.* **1996**, *100*, 12735.
(74) Gruebele, M. *Theor. Chem. Acc.* **2003**, *109*, 53.
(75) Liu, Y.; Lohr, L. L.; Barker, J. R. *J. Phys. Chem. B* **2005**, *109*, 8304.
(76) Keshavamurthy, S. *Int. Rev. Phys. Chem.* **2007**, *26*, 521.
(77) Car, R.; Parrinello, M. *Phys. Rev. Lett.* **1985**, *55*, 2471.
(78) Remler, D. K.; Madden, P. A. *Mol. Phys.* **1990**, *70*, 921.
(79) Tuckerman, M. E.; Parrinello, M. *J. Chem. Phys.* **1994**, *101*, 1302.
(80) Andersen, H. C. *J. Chem. Phys.* **1980**, *72*, 2384–2393.
(81) Parrinello, M.; Rahman, A. *Phys. Rev. Lett.* **1980**, *45*, 1196–1199.
(82) Petersen, M. K.; Iyengar, S. S.; Day, T. J. F.; Voth, G. A. *J. Phys. Chem. B* **2004**, *108*, 14804–14806.
(83) Golub, G. H.; Loan, C. F. V. *Matrix Computations*; The Johns Hopkins University Press: Baltimore, 1996.
(84) Swope, W. C.; Andersen, H. C.; Berens, P. H.; Wilson, K. R. *J. Chem. Phys.* **1982**, *76*, 637.
(85) Pulay, P. *Mol. Phys.* **1969**, *17*, 197.
(86) Trotter, M. F. *Proc. Am. Math. Soc.* **1959**, *10*, 545.
(87) Nelson, E. *J. Math. Phys.* **1964**, *5*, 332.
(88) Czako, G.; Kaledin, A. L.; Bowman, J. M. *J. Chem. Phys.* **2010**, 132.
(89) Bowman, J. M.; Gazdy, B.; Sun, Q. Y. *J. Chem. Phys.* **1989**, *91* (5), 2859.
(90) Miller, W. H.; Hase, W. L.; Darling, C. L. *J. Chem. Phys.* **1989**, *91*, 2863.
(91) Riesz, F.; Sz.-Nagy, B. *Functional Analysis*; Dover Publications, Inc.: New York, 1990.
(92) Kawaguchi, K. *J. Chem. Phys.* **1988**, *88*, 4186–4189.
(93) Gudeman, C.; Begemann, M.; Pfaff, J.; Saykally., R. J. *Phys. Rev. Lett.* **1983**, *50*, 727.
(94) Saykally, R. *Science* **1988**, *239*, 157.
(95) McQuarrie, D. A.; Simon, J. D. *Physical Chemistry: A Molecular Approach*; University Science Books: CA, 1997.
(96) Iyengar, S. S. *Theor. Chem. Acc.* **2006**, *116*, 326.
(97) Jakowski, J.; Sumner, I.; Iyengar, S. S. *J. Chem. Theory Comput.* **2006**, *2*, 1203–1219.
(98) Li, X.; Iyengar, S. S. *J. Phys. Chem. A* **2011**, *115*, 6269.
(99) Li, X.; Iyengar, S. S. *J. Chem. Phys.* **2010**, *133*, 184105.
(100) Hocker, D.; Li, X.; Iyengar, S. S. *J. Chem. Theory Comput.* **2011**, *7*, 256.